Hindawi
Structural Control and Health Monitoring
Volume 2024, Article ID 5532909, 22 pages
https://doi.org/10.1155/2024/5532909

Research Article

A Physics-Informed Neural Network for the Nonlinear Damage Identification in a Reinforced Concrete Bridge Pier Using Seismic Responses

Takahiro Yamaguchi and Tsukasa Mizutani

Institute of Industrial Science, The University of Tokyo, 4-6-1, Komaba, Meguro-ku, Tokyo 153-8505, Japan

Correspondence should be addressed to Takahiro Yamaguchi; tyamag@iis.u-tokyo.ac.jp

Received 1 December 2023; Revised 23 January 2024; Accepted 1 February 2024; Published 9 February 2024

Academic Editor: Chia-Ming Chang

The condition assessment of reinforced concrete (RC) bridge piers after an earthquake using measured responses is important for ensuring the safety of road and railway users. The problem is nonlinear, and the locations and extents of damages are various. However, previous research works focused on linear structural identification or model updating assuming a limited number of nonlinear materials for reasonable estimates. Leveraging the ability of deep learning (DL) for robustly estimating a large number of unknown parameters, this study proposes an ALL nonlinear spring multi-degree-of-freedom (MDOF) damage identification algorithm based on a physics-informed neural network (PINN). The algorithm is applied to a stacked bilinear rotational spring and damper model of a pier. The number of unknown parameters reaches about 50. The errors of estimated elastic stiffnesses, damping coefficients, and ductility factors (DFs) using simulated responses added with noises are 0.4%, 0.6%, and 3.1%, respectively. Using full-scale RC bridge pier shaking table experiments, the algorithm revealed the distributions of elastic stiffnesses and DFs along the pier height and their deteriorations. The effects of different types of local damages are quantitatively evaluated and visualized on the distributions.

1. Introduction

Ensuring the safety of transportation infrastructures in hazards is essential for evacuation and following restoration. Also, to efficiently rehabilitate enormous amounts of infrastructures, monitoring and evaluating the conditions are key steps.

This study focuses on reinforced concrete (RC) bridge piers after seismic events. RC bridge piers are prevailing and critical components for road and railway bridges. Many east and middle east Asian, American, and African countries have recently suffered from large earthquakes such as Tohoku earthquake in 2011, Nepal earthquake in 2015, and Turkey-Syria earthquake in 2023 to name a few, causing devastating collapses of structures [1, 2].

A lesson from Kobe (Great Hanshin) earthquake in 1995 is that there are two types of failure modes in RC bridge piers, i.e., shear and flexural failure. Shear failure is dangerous because it is not redundant. This lesson has been reflected in the Japanese standard design [3].

Even though a flexure-dominant behavior is assumed, the problem is nonlinear, and the locations and extents of damages are various depending on the dynamic characteristics of piers and input ground motions. For example, a typical local damage is spalling of concrete in the bottom of a pier just above the foundation. The spalling can spread in horizontal and height directions. Cracks can occur anywhere in the pier and progress during the seismic event. Rebars around the spalling and cracks may yield and be debonded. This study does not target long-term deteriorations, e.g., corrosion of rebars, deficiency of bearings, and scouring. However, this study considers stiffnesses. Therefore, the current condition of the pier is reflected in the estimated stiffnesses.

There have been large advancements in dynamic monitoring methods and computational environments. For example, a wireless multihop accelerometer network enables dense monitoring of large structures [4]. Image analysis by deep learning (DL), sampling-moire, 8k cameras, and terrestrial laser scanner (TLS) processing algorithms offer high-resolution displacement data [5–9]. Strain can be also estimated [10]. With the advent of DL technologies, big data can be analyzed by neural networks (NNs) using the graphic processing unit (GPU) [11, 12]. GPUs are also applied to computationally intensive simulations. However, in the opinion of the authors, these dense monitoring data and efficient analysis methods are not fully utilized in structural identification.

The motivation of this study is to localize and quantify deteriorations in a bridge pier by estimating dynamic properties using measured seismic responses. Linear or a small number of nonlinear materials are not enough to realize this motivation. The novelty of this study is the damage identification of an ALL nonlinear spring and damper multi-degree-of-freedom (MDOF) system by a proposed physics-informed neural network (PINN) inverse analysis scheme. Multiple physical quantities are considered as measurement data. The maximum number of unknown parameters is 48. To the best of the authors' knowledge, the problem is the most challenging among the previous research works, resulting in the abandonment of traditional modal and machine learning (ML) methods and proposal of the PINN-based method. This point is detailed in the following section.

The outline of this article is as follows: Section 2 is a literature review related to RC bridge pier evaluation and PINN. Section 3 summarizes a problem setting showing an assumed dynamic model, and Section 4 proposes the algorithm. Section 5 explains a simulation case and characteristic features of simulated responses. Section 6 validates the algorithm and conducts parametric studies using simulations. Section 7 validates the algorithm using the measured responses of full-scale shaking table experiments. Section 8 summarizes the contributions of this study and discusses limitations for future work. Section 9 concludes the article.

2. Literature Review and Contributions

This section discusses three aspects related to the dynamic analysis of RC bridge piers: structural identification and damage evaluation algorithms for piers and piers with other structural components, state-of-the-art inverse analysis by PINN, and dynamic characteristics and modelling of RC piers. A dynamic model is important because it is incorporated into the proposed PINN damage identification algorithm.

The classic of modal identification, natural excitation technique, and eigensystem realization algorithm (NExT-ERA) was introduced by Caicedo et al. based on matrix decomposition techniques [13]. Chang and Pakzad modified NExT to apply to stochastic data [14]. Siringoringo and Fujino applied system realization using the information matrix (SRIM), one of the system identification schemes to seismic records of cable-stayed bridges [15]. Loh and Lee applied a local structure system identification method to the measurement data of a multispan pier-deck system to evaluate detailed dynamic properties of the bridge components [16]. These algorithms are robust to measurement noises. However, they are limited to a linear problem in their nature.

Another approach is a frequency-domain method. Chaudhary et al. adopted a loss function based on a natural frequency and damping factor [17]. Dynamic properties were estimated by minimizing the loss function using a thorough search with assumed parameter ranges. Chaudhary et al. applied the algorithm to a soil-structure interaction problem [18]. Yoshida et al. estimated the dynamic properties of a single-degree-of-freedom (SDOF) mass-spring-damper system using viaduct responses in Kobe earthquake [19]. The gap of a transfer function was minimized. Frequency-domain methods also assume that a target problem is linear.

For considering nonlinear structural identification, the number of unknown parameters should be limited to obtain reasonable solutions. Huang et al. estimated nonlinear dynamic properties of an isolation system between a deck and pier using a gradient descent approach [20]. Ebrahimian et al. also applied a gradient descent algorithm for estimating nonlinear material parameters from responses [21]. They assumed a multistory building with column and beam two material parameter sets. In noisy environments, the errors of the converged parameters were a few tens percent.

Kalman filter (KF) approaches are related to this study in that they are applicable to nonlinear problems, and the dynamics of a system and measurement data are simultaneously considered. Chatzis et al. applied an unscented KF to estimate modal parameters of a multistory building specimen [22]. Yang et al. adopted an extended KF to estimate two stiffnesses and damping factors of a pier-pile-soil interaction system [23]. The later work considered the varying features of the stiffnesses. However, no nonlinear hysteretic model was discussed. Furthermore, there were up to 50% gaps between target and estimated parameters and the same amounts of fluctuations until they converged. DL has an advantage in estimating a large number of unknown parameters.

To open a new horizon of structural identification, the authors focus on a PINN for inverse analysis. Milestone achievements by Raissi et al. and Jagtap et al. were PINNs for forward and inverse analysis of nonlinear fluid partial differential equations [24–26]. Haghighat et al. applied a PINN inverse analysis scheme to perforated plate stress reproduction [27]. These research works estimated parameters of governing equations and distributions of responses with limited training data samples. In terms of response reproduction, Li et al. applied a PINN to a simple beam [28]. Zhang et al. considered a nonlinear frame structure [29]. PINN is novel; there is no example of structural identification except for simple components such as a beam and plate. This study formulates a nonlinear MDOF RC bridge pier damage identification problem based on PINN from scratch.

Different strategies can be adopted if the damage evaluations of piers are only targeted. A recent trend is the application of machine learning (ML) and DL to the damage predictions of structures. Todorov and Muntasir Billah proposed a ML-based algorithm to correlate conditions such as concrete spalling and rebar buckling with input ground motions [30]. Achieved R^2 was 0.5–0.7, implying the difficulty of the problem. Fernandez-Navamuel et al. trained an NN using the finite element method (FEM) to predict the severity of deck elements provided by dynamic responses [31]. Anastasopoulos et al. proposed a regression model for predicting responses using input seismic intensity measures [32]. Ahmadi et al. proposed an anomaly detection algorithm based on short-time Fourier transform (STFT) for identifying damaged piers in a bridge [33]. In some of these approaches, the applicability and robustness of the developed algorithms to other bridges were not clear. Furthermore, the interpretation of the severity output by the algorithms was needed for practical application.

To realize the PINN, the appropriate modelling of a nonlinear RC bridge pier behavior is essential. Insights on modelling nonlinear hysteretic curves of structures are summarized in [34, 35]. Kim et al. developed an analytical nonlinear RC pier model to correlate the local deteriorations of materials and responses of the whole structure [36]. Oller and Barbat incorporated a damage model into an RC pier section model for accurate moment-curvature analysis [37].

This study adopts the simplest bilinear hysteresis model with elastic and second stiffnesses and a yield point. This is because the model can reproduce nonlinear local damages with the minimum number of unknown parameters. Typical RC piers show complicated skeleton curves such as trilinear and modified Takeda models. The application of other models is left for future work.

The modelling of this study is inspired by [38–40], which proposed pier and foundation pile models combining sway-rock springs between lumped masses. To reproduce a flexure behavior of a pier, this study adopts a link model with rocking springs and dampers between lumped masses instead of a frame model. The reason is detailed in the following section. Okada et al. approximated Japanese standard RC bridge piers using sway-rock models [40]. They indicated that pier and pile horizontal spring stiffnesses are $1 \cdot 10^8$-$1 \cdot 10^9$ N/m. Considering a 1-2 m height component, equivalent rotational stiffnesses are around $1 \cdot 10^9$ N. This value is referred in Section 5–7.

The concept of the damage identification method proposed in this study is novel which is motivated from the previous research works on PINN. The first contribution is that PINN equations for a nonlinear MDOF RC bridge pier dynamic model are derived. A damage identification scheme is developed using a deep NN, measured responses, loss function, and dynamic parameter update rules (Section 3 and 4). The second contribution is that the proposed PINN algorithm is validated using simulated responses added with noises. The robustness of the algorithm to the number of measurement data points, noises, and ground motions is demonstrated. The effects of NN parameters and required physical quantities are discussed for practical application (Sections 5 and 6).

Besides simulations, to demonstrate the applicability of the algorithm, experimental data are important. Sideris et al. developed a 1 : 2.4 pier-deck specimen to confirm the behavior of the system under different seismic excitations [41]. Chen et al. developed a 1/7-scale tall-height pier specimen considered in mountainous areas in China [42]. Kang et al. developed a pier-deck specimen to evaluate the performance of a high-speed railway bridge [43].

This study adopts experimental data publicly offered by Kawashima et al. [44]. The unique feature of this experiment, called E-Defense, is full-scale shaking table tests using an RC bridge pier following the recent Japanese standard (Figure 1). A Kobe earthquake seismic wave was applied to the specimen. Controlled excitors and supporting facilities were developed. Accelerations, velocities, displacements, and movies were obtained with a detailed damage inspection report. Related to E-Defense, Takahashi and Kobayashi evaluated the statistical variations of 16 RC bridge pier specimens [45].

The third contribution is that the algorithm is applied to full-scale RC bridge pier shaking table experiment data. The algorithm can output the distributions of elastic stiffnesses and ductility factors (DFs) in a pier height direction. Inspection results are related to these indices to demonstrate the ability of the algorithm for evaluating different types of local damages (Section 7).

Other important aspects which should be discussed are as follows: probabilistic approaches are another trend in structural engineering, which are intended for the accurate prediction of pier performances. Karim and Yamazaki developed fragility curves based on simulation results changing input seismic excitations [46]. Dhakal et al. designed input acceleration spectra to predict possible ranges of displacements [47]. NN can be easily advanced to a probabilistic model adopting a Bayesian approach [48]. Roy et al. compared the behaviors of pier simulation models with unidirectional and bidirectional shaking inputs [49]. Unidirectional analysis is valid considering a principal direction. On the other hand, there is a possibility that three-dimensional (3D) distributions of damages may be estimated utilizing bidirectional responses obtained at multiple measurement points in horizontal sections. These directions remain as promising future work.

3. Dynamic Model and Solver

This section discusses a dynamic model assumed in the PINN and simulations. PINN is applicable to any physical problems changing the assumed model. Inverse analysis by PINN is a process to balance fidelity to the measured responses and dynamic model. The parameters of the model are updated as much as possible to approximate responses. Therefore, the model should be precise enough to reproduce the responses with fewer parameters.

Previous link models are limited to linear systems [38–40]. Nonlinear MDOF systems are rarely discussed possibly because of the complexity of the systems. Therefore, equations are derived here, and characteristic features are discussed in Section 5.

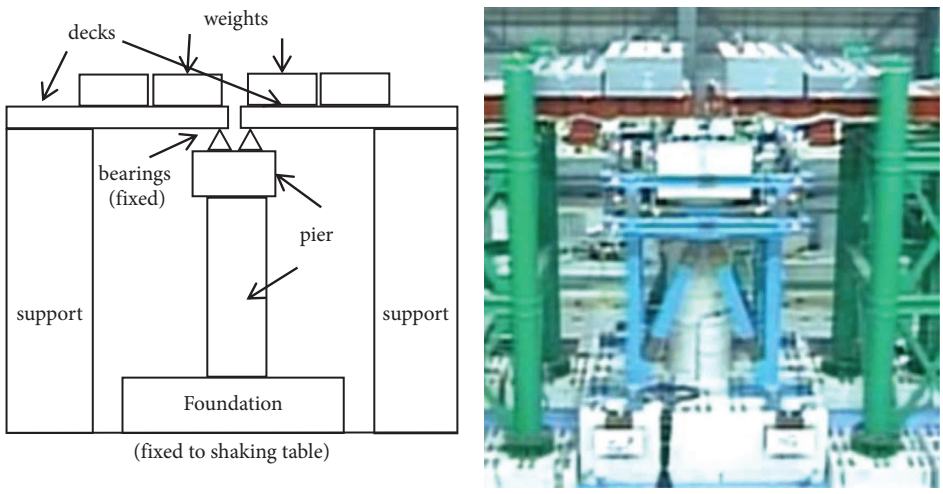

Figure 1: E-defense RC bridge pier specimen from [43]. (a) Schematic of the pier. (b) Photo. Loads of discontinuous decks and weights are transferred to the pier via fixed bearings. The foundation is fixed to the shaking table.

3.1. Dynamic Model. Figure 2(a) summarizes the model. The model consists of N-lumped masses connected with N rotational springs and N rotational viscous dampers. In order to model a flexure behavior, only rotational springs are assumed. Shear springs and shear dampers can be also introduced. If a frame element with Young's modulus E, moment of inertia I, and length h is assumed, equivalent rotational stiffness k is written as follows:

$$k = \frac{\mathrm{EI}}{h}. \tag{1}$$

Therefore, the link and frame models are equivalent. The two reasons for adopting the link model are to reduce the number of the parameters and to clarify that the problem addressed by the PINN is the reproduction of discrete responses and optimization of discrete parameters using a mass-spring-damper system.

The model assumes that the foundation is fixed to the ground. It was reported that certain combinations of soil and pile dynamic characteristics caused large sway-rocking motions of foundations and piles [50, 51]. They are ignored in this study for simplicity. The ground is subjected to horizontal excitation acceleration $\ddot{x}_e$. The foundation can be fixed assuming that inertial force F_n is applied to each mass m_n:

$$F_n = -m_n \ddot{x}_e. \tag{2}$$

To apply this assumption, the acceleration of the foundation should be measured. Measurement data should be relative responses, or foundation responses should be subtracted from the measurement data. The discussion here is considering the relative responses between each mass and the foundation.

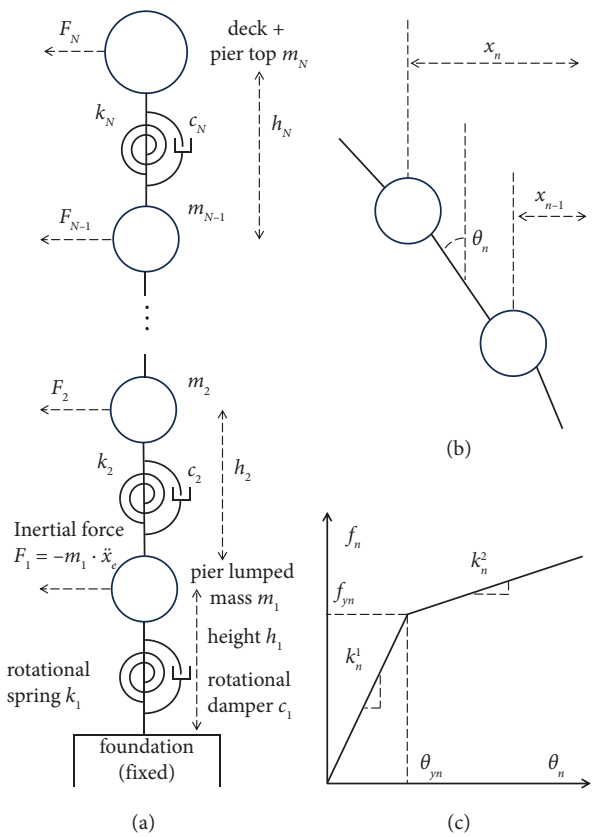

Figure 2: Schematic of the dynamic model. (a) Link model with lumped masses and rotational springs and dampers. (b) Displacements of masses and angles of springs. Note that responses are displacements, while the behaviors of springs are described with angles. (c) Nonlinear spring characterized with two stiffnesses and a yield moment. Hysteretic curves are constrained by skeleton curves with the nonlinear parameters.

The pier above the foundation is divided into multiple masses according to measurement points. Any division is possible in the PINN though it may increase the difficulty. The displacements of masses in a height direction are assumed to be small. The deck and portion of the pier top are approximated to one mass because our target is not a bearing. However, bearings have different dynamic characteristics. This fact affects the top stiffness k_N as will be discussed in Section 7.

The rotations of springs cause horizontal motions of masses (Figure 2(b)). The inclination of the pier accumulates in the upper part of the pier. The angle of each spring θ_n from an equilibrium state is formulated using displacement of each mass x_n and height of each spring connecting two masses h_n:

$$\theta_1 = \frac{x_1}{h_1}, \tag{3}$$

$$\theta_2 = \frac{(x_2 - x_1)}{h_2} - \frac{x_1}{h_1}, \tag{4}$$

$$\theta_n = \frac{(x_n - x_{n-1})}{h_n} - \frac{(x_{n-1} - x_{n-2})}{h_{n-1}} \; (3 \le n \le N), \tag{5}$$

x_n and θ_n are the responses of the n-th mass and n-th spring. In this article, a bold character means that n states of all the masses are aligned in a vector. Displacements and angles of the pier are represented by $\mathbf{x}$ and $\boldsymbol{\theta}$. This displacement-angle relationship is important because what we can observe is $\mathbf{x}$, while the nonlinearity of springs is defined with $\boldsymbol{\theta}$.

The restoring moment f_n of the spring assuming yield moment f_{yn}, yield angle θ_{yn}, elastic (first) rotational stiffness k_n^1, and second (plastic) rotational stiffness k_n^2 is described as follows (Figure 2(c)):

$$f_n^1 = k_n^1 \theta_n, \tag{6}$$

$$f_n^2 = k_n^2 \left(\theta_n - \theta_{\mathrm{yn}}\right) + f_{\mathrm{yn}}, \tag{7}$$

$$f_n = \mathrm{median}\left(\left[-f_n^2, f_n^1, f_n^2\right]\right). \tag{8}$$

Note that k_n is not a shear but a rotational spring stiffness. This nonlinear modelling is the same as an ordinary bilinear shear spring [34, 35]. f_n is bounded by a skeleton curve defined by f_{yn}. At any θ_n, $|f_n|$ should not exceed $|f_n^2|$. This model is elastic inside the boundary and plastic on the boundary. f_{yn} determines whether the spring is in linear or nonlinear ranges at given time t. k_n^2 is typically one digit smaller than k_n^1.

As a summary, response set $\mathbf{T}$ consists of displacement $\mathbf{x}$, velocity $\dot{\mathbf{x}}$, acceleration $\ddot{\mathbf{x}}$, and restoring moment $\mathbf{f}$ at each time t and all n. T is a matrix $(\ddot{\mathbf{x}}(\mathbf{t}), \dot{\mathbf{x}}(\mathbf{t}), \mathbf{x}(\mathbf{t}), \mathbf{f}(\mathbf{t}))$. Viscous damping c_n is considered for an angular velocity. The parameter set $\mathbf{K}$ to be optimized is $\mathbf{K} = (\mathbf{k^1}, \mathbf{k^2}, \mathbf{f_y}, \mathbf{c})$.

3.2. Governing Equations. This subsection derives governing equations. Typical PINNs have boundary conditions (BCs, [24–26]). BCs $\mathbf{T_b}$ for $\mathbf{T}$ can be considered by minimizing $\sum_{n,t}|\mathbf{T} - \mathbf{T_b}|^2$ in a PINN loss function. In this study, because there are many loss terms, the BCs are included in the governing equations for simplicity. For example, the foundation should be fixed. Displacement of the foundation $x_0 = 0$. This condition is included in equation (3) assuming $\theta_1 = (x_1 - x_0)/h_1$. This approach is different from minimizing $\sum_{n,t}|\mathbf{T} - \mathbf{T_b}|^2$ because the latter does not necessarily follow the BCs. This study assumes that the BCs are fundamental and exactly satisfied. Measured responses are incorporated into the loss function in the previous and these studies. Therefore, the responses are also considered as types of BCs in the context of PINN.

Governing equations of the model in Figure 2(a) can be derived by considering the equilibrium of moments at each mass. This study uses a Euler–Lagrange equation for simple derivation [52, 53]. The results are the same as those derived from the equilibrium of moments. Kinetic energy T_E and potential energy U_E of masses, springs, and dampers are written as follows:

$$T_E = \sum_n \left\{\frac{1}{2} m_n (\dot{x}_n)^2 + \frac{1}{2} c_n \left(\dot{\theta}_n\right)^2\right\}, \tag{9}$$

$$U_E = \sum_n \frac{1}{2} k_n (\theta_n)^2. \tag{10}$$

Using Lagrangian $L_E = T_E - U_E$ and an inertial force on each mass caused by a seismic wave F_n, the Euler–Lagrange equation is written as follows:

$$\frac{d}{\mathrm{dt}}\left(\frac{\partial L_E}{\partial \dot{x}_n}\right) - \frac{\partial L_E}{\partial x_n} = F_n. \tag{11}$$

Detailed derivation is skipped for brevity. Using equations (3)–(11), the governing equation is derived below in a similar formula as an MDOF equation of motion:

$$\mathrm{M}\ddot{\mathbf{x}} + \mathrm{C}\dot{\mathbf{x}} + \mathrm{R}\mathbf{f} = \mathbf{F}. \tag{12}$$

The mass matrix M, damping matrix C, and restoring moment conversion matrix R are defined in the following equations:

$$M = \mathrm{diag}(m_1, m_2, \ldots m_N), \tag{13}$$

$$C = \begin{pmatrix} \left(\frac{1}{h_1}\right)^2 c_1 + \left(\frac{1}{h_1}+\frac{1}{h_2}\right)^2 c_2 + \left(\frac{1}{h_2}\right)^2 c_2 & -\frac{1}{h_2}\left(\frac{1}{h_1}+\frac{1}{h_2}\right)c_2 - \frac{1}{h_2}\left(\frac{1}{h_2}+\frac{1}{h_3}\right)c_3 & \frac{1}{h_2}\frac{1}{h_3}c_3 & 0 & \cdots & 0 \\ -\frac{1}{h_2}\left(\frac{1}{h_1}+\frac{1}{h_2}\right)c_2 - \frac{1}{h_2}\left(\frac{1}{h_2}+\frac{1}{h_3}\right)c_3 & \left(\frac{1}{h_2}\right)^2 c_2 + \left(\frac{1}{h_2}+\frac{1}{h_3}\right)^2 c_3 + \left(\frac{1}{h_3}\right)^2 c_3 & -\frac{1}{h_3}\left(\frac{1}{h_2}+\frac{1}{h_3}\right)c_3 - \frac{1}{h_3}\left(\frac{1}{h_3}+\frac{1}{h_4}\right)c_4 & \frac{1}{h_3}\frac{1}{h_4}c_4 & 0 & \cdots \\ \vdots & \vdots & \vdots & \vdots & \vdots & \ddots \\ 0 & \cdots & 0 & 0 & \frac{1}{h_{N-1}}\frac{1}{h_N}c_N & -\frac{1}{h_N}\left(\frac{1}{h_{N-1}}+\frac{1}{h_N}\right)c_N \end{pmatrix} \begin{matrix} 0 \\ 0 \\ \vdots \\ \left(\frac{1}{h_N}\right)^2 c_N \end{matrix}, \tag{14}$$

$$R = \begin{pmatrix} \frac{1}{h_1} & -\left(\frac{1}{h_1}+\frac{1}{h_2}\right) & \frac{1}{h_2} & 0 & \cdots & 0 \\ 0 & \frac{1}{h_2} & -\left(\frac{1}{h_1}+\frac{1}{h_2}\right) & \frac{1}{h_3} & 0 \cdots & 0 \\ & & & \ddots & & \vdots \\ \vdots & \vdots & & & & \\ 0 & \cdots & & 0 & \frac{1}{h_3} & \end{pmatrix}. \tag{15}$$

Equation (14) seems complicated. Actually, the calculation of R$\mathbf{f}$ in equation (12) is most complicated because equations (3)–(8) should be considered for converting $\mathbf{x}$ to $\mathbf{f}$. If there are shear springs and shear dampers, terms are added to the left side of equation (12).

3.3. Solver. In the PINN, a solver is incorporated into the loss function. Also, simulations are utilized in this study. Therefore, this subsection describes the solver for calculating the responses of equations (12)–(15).

Equations (12)–(15) describe the governing equations, and equations (3)–(8) are related to the nonlinear material properties of the springs. There are some algorithms to solve nonlinear partial differential equations such as the Runge–Kutta method and the central difference scheme [54, 55]. This study applies the Newmark-β method as one of the most typical solvers in structural engineering. This study adopts the linear acceleration method ($\gamma = 1/2$ and $\beta = 1/6$). Accelerations, velocities, and displacements at t are estimated using the three responses at $t - \mathrm{dt}$:

$$\ddot{\mathbf{x}}(t) = \left(M + \frac{\mathrm{dt}}{2}C\right)^{-1} * \left\{-\mathrm{M}\mathbf{F}(t) - \mathrm{R}\mathbf{f}(t) - C\left(\dot{\mathbf{x}}(t-\mathrm{dt}) + \frac{\mathrm{dt}}{2}\ddot{\mathbf{x}}(t-\mathrm{dt})\right\}, \tag{16}$$

$$\dot{\mathbf{x}}(t) = \dot{\mathbf{x}}(t-\mathrm{dt}) + \frac{\mathrm{dt}}{2}\left(\ddot{\mathbf{x}}(t-\mathrm{dt}) + \ddot{\mathbf{x}}(t)\right), \tag{17}$$

$$\mathbf{x}(t) = \mathbf{x}(t-\mathrm{dt}) + \frac{\mathrm{dt}}{2}\dot{\mathbf{x}}(t-\mathrm{dt}) + \frac{(\mathrm{dt})^2}{3}\ddot{\mathbf{x}}(t-\mathrm{dt}) + \frac{(\mathrm{dt})^2}{6}\ddot{\mathbf{x}}(t). \tag{18}$$

Two problems in applying the Newmark-β method are the estimation of $\mathbf{f}(t)$ and determination of dt. $\ddot{\mathbf{x}}(t)$ is estimated using $\mathbf{f}(t)$ via equation (16). $\mathbf{f}(t)$ is estimated using $\mathbf{x}(t)$ via equations (3)–(8). $\mathbf{x}(t)$ is estimated using $\ddot{\mathbf{x}}(t)$ via equation (18). Therefore, $\mathbf{x}$ and $\mathbf{f}$ were mutually updated until they converged. It was observed that updating them twice leads to changes less than 0.01%. Assumed dt = 0.001 is one tenth smaller than the sampling frequency of the measurements 100 Hz.

4. PINN for Nonlinear MDOF Mass-Spring-Damper System Identification

Figure 3 summarizes the concept of the proposed PINN for dynamic system identification. NN outputs predicted responses $\mathbf{T_p}$. Simultaneously, the PINN has measured responses $\mathbf{T_m}$ and governing equations FM. FM includes input accelerations. These factors constitute loss function L. By minimizing L, the parameters of the NN and dynamic model are simultaneously optimized. In other words, the PINN estimates dynamic parameters referring to governing equations and measurement data. However, the PINN does not completely follow the governing equations or measurement data. The advantage of the PINN is data assimilation utilizing DL for accurate and robust inverse analysis. One update using the whole $\mathbf{T_m}$ corresponds to one epoch. The update is also called "training" in the NN. The inverse analysis scheme proposed in this study is novel which is motivated by the previous PINN-related research works [24–28]. The derivation of nonlinear dynamic model losses, regularization factors, and update rules of dynamic parameters are discussed.

The problem setting in this study is clarified here referring to Figure 3 and the discussions of the dynamic model in the previous section. Measurement data are the seismic responses of an RC bridge pier. Acceleration $\ddot{x}$, velocity $\dot{x}$, displacement x, and restoring moment f at each measurement position n and time t are considered. The PINN can consider inhomogeneous data in spatial and time directions. This study focuses on homogeneous data. In practice, it is difficult to measure f. A workaround is shown in Section 4.4. Estimation targets are elastic and second stiffness k_n^1, k_n^2, yield moment f_{yn}, and damping coefficient c_n of the bilinear rotational springs and dampers between the measurement positions. The PINN also reproduces responses. Considering the reproduced responses and dynamic parameters, any damage indices can be evaluated. Appropriate indices are discussed in Section 4.5.

The algorithm consists of four parts: NN, dynamic model, measurement, and loss function. The combination of the NN and dynamic model is the PINN. The dynamic model is explained in Section 3. The NN, loss function, and optimization of the loss function are detailed in the following subsections.

4.1. Neural Network. There are two points to be customized in the NN for the considered problem. The first point is that the input of the network is only t for simplicity. Previous PINNs also use n as an input [24–28]. In this study, only limited n is considered. Furthermore, this study focuses not only on the distributions of responses along the pier height but also on the dynamic parameters. The second point is that this study adopts a dynamical model. The relationship among different quantities at different times defined by the Newmark-β method and nonlinear spring hysteresis is introduced in L. Therefore, $\mathbf{T_p}(t)$ should be responses at all positions and time fractions t and $t + \Delta t$:

$$\mathbf{T_p} = \left\{\ddot{x}_{1p}(t), \ldots, \ddot{x}_{\mathrm{Np}}(t), \ddot{x}_{1p}(t+\Delta t), \ldots, \ddot{x}_{\mathrm{Np}}(t+\Delta t), \ldots, f_{1p}(t), \ldots, f_{\mathrm{Np}}(t), f_{1p}(t+\Delta t), \ldots, f_{\mathrm{Np}}(t+\Delta t)\right\}. \tag{19}$$

This formulation is similar to a state space model. $\mathbf{T_p}$ is states. $\mathbf{T_p}$ should be close to $\mathbf{T_m}$ and simultaneously follow the dynamic model $\mathrm{FM}(\mathbf{K}, \mathbf{T_p}) = 0$. This study compares multiple combinations of physical quantities. In the case of measuring $\ddot{x}$, $\dot{x}$, x, and f at N positions and t and $t + \Delta t$, the total number of outputs is $8N$. The number of the outputs is large compared to the previous PINNs to incorporate hysteretic nonlinearity.

Figure 4 depicts the architecture of the adopted NN. The architecture follows the regression networks of the previous PINNs [24, 25]. The architecture is a cascade of q fully connected layers. The input is connected to p perceptrons. The outputs of the perceptrons go through activation functions. The rectified linear unit (ReLU) is adopted as the activation functions. To avoid gradient vanishing and exploding, batch normalization is applied to the outputs of the ReLU. The outputs are input to the next fully connected layer. The outputs of the q-th layer are connected to the final $8N$ perceptron layer to predict $8N$ responses.

The NN parameters are p and q. There is a tradeoff. The NN approximated the time histories of the responses as functions of t using deep fully connected layers. It was reported that deep fully connected layers have a high ability to represent nonlinear chaotic signals [56]. The smaller p, q are, the inferior the representation ability of the NN is. On the other hand, the larger p, q are, the higher computational cost is. p, q are selected confirming the convergence of the loss. This point will be discussed in Section 6.3.2. Instead of training one NN, multiple separate NNs can be trained for predicting parts of the $8N$ responses. The previous research works indicated separating NNs improves prediction results [24–28]. However, it was not effective in this study possibly because of the high correlations among the responses.

4.2. Loss Function. Predicted responses $\mathbf{T_p}$ and measured responses $\mathbf{T_m}$ are obtained. The physical quantities of $\mathbf{T_m}$ should correspond to $\mathbf{T_p}$. This study adopts the mean square error (MSE). In loss function L, the gap between the predicted and measured responses $(\mathbf{T_p} - \mathbf{T_m})^2$ is minimized. The dynamic model FM = 0 defines the relationship among the dynamic parameters $\mathbf{K}$ and predicted responses $\mathbf{T_p}$. Therefore, FM^2 should be minimized. The MSEs are summed up to construct L.

To be specific, the formulas of FM and L are derived in the case that $\ddot{x}(t)$, $\dot{x}(t)$, $x(t)$, and $f(t)$ are observable. All responses are discrete in spatial and temporal directions. $\ddot{x}_{\mathrm{np}}(t)$, $\dot{x}_{\mathrm{np}}(t)$, $x_{\mathrm{np}}(t)$, and $f_{\mathrm{np}}(t)$ are predictions, and

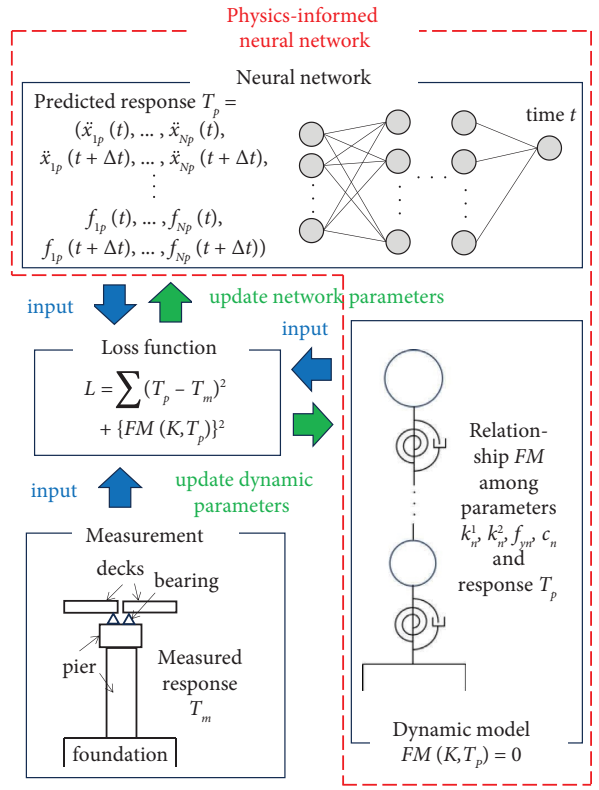

Figure 3: Concept of the PINN for bridge pier dynamic system identification. The algorithm is composed of the NN, dynamic model, measurement, and loss function. The combination of the NN and dynamic model is called the PINN. The NN prediction, measurement data, and dynamic model are input to the loss function. The loss function is minimized to optimize the NN and dynamic parameters simultaneously.

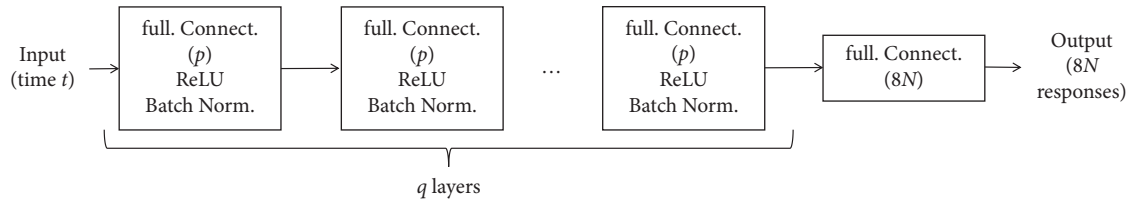

Figure 4: Architecture of the NN. The architecture follows the previous research works [24–28]. The input is time t. q fully connected layers with p perceptrons and one fully connected layer with $8N$ perceptrons are connected to output $8N$ responses. An ReLU activation function and batch normalization are applied to each layer output to prevent gradient vanishing and exploding problems.

$\ddot{x}_{nm}(t)$, $\dot{x}_{nm}(t)$, $x_{nm}(t)$, and $f_{nm}(t)$ are measurements. The gaps are defined as follows:

$$L_1 = \alpha_1 \sum_{n,t} \left(\ddot{x}_{np} - \ddot{x}_{nm}\right)^2 + \alpha_2 \sum_{n,t} \left(\dot{x}_{np} - \dot{x}_{nm}\right)^2 + \alpha_3 \sum_{n,t} \left(x_{np} - x_{nm}\right)^2 + \alpha_4 \sum_{n,t} \left(f_{np} - f_{nm}\right)^2, \tag{20}$$

α_1–α_4 are regularization factors. The gaps are summed up for every set at (n, t). Therefore, each set is considered as one of the training datasets.

The predicted responses should follow the dynamic model at t:

$$L_2 = \alpha_5 \sum_{n,t} (\mathrm{M}\ddot{\mathbf{x}} + \mathrm{C}\dot{\mathbf{x}} + \mathrm{R}\mathbf{f} - \mathbf{F})^2. \tag{21}$$

This study incorporates the incremental scheme of the Newmark-β method into L:

$$L_3 = \alpha_6 \sum_{n,t} \left[\ddot{\mathbf{x}}(t+\Delta t) - \left(M + \frac{\Delta t}{2} C \right)^{-1} * \left\{ -\mathrm{M}\mathbf{F}(\mathbf{t}+\Delta\mathbf{t}) - \mathrm{R}\mathbf{f}(t+\Delta t) - C\left(\dot{\mathbf{x}}(t) + \frac{\Delta t}{2}\ddot{\mathbf{x}}(t)\right) \right\} \right]^2, \tag{22}$$

$$L_4 = \alpha_7 \sum_{n,t} \left[\dot{\mathbf{x}}(t+\Delta t) - \dot{\mathbf{x}}(t) - \frac{\Delta t}{2} \left(\ddot{\mathbf{x}}(t) + \ddot{\mathbf{x}}(t+\Delta t) \right) \right]^2, \tag{23}$$

$$L_5 = \alpha_8 \sum_{n,t} \left[\mathbf{x}(t+\Delta t) - \mathbf{x}(t) - \frac{\Delta t}{2}\dot{\mathbf{x}}(t) - \frac{(\Delta t)^2}{3}\ddot{\mathbf{x}}(t) - \frac{(\Delta t)^2}{6}\ddot{\mathbf{x}}(t+\Delta t) \right]^2. \tag{24}$$

The nonlinearity of the springs is also included:

$$L_6 = \alpha_9 \sum_{n,t} \left[f_n(t) - \mathrm{median}\left(\left[-f_n^2(t), f_n^1(t), f_n^2(t) \right] \right) \right]^2, \tag{25}$$

f_n^1 and f_n^2 are defined in equations (6) and (7). The summed up loss function L is

$$L = L_1 + L_2 + L_3 + L_4 + L_5 + L_6, \tag{26}$$

L is the objective function. L is divided by the number of datasets for convenience of discussions.

Any loss functions can be added to the right side of equation (26). On the other hand, no term in Eq. (26) is removable in the considered problem. Measurement data are considered via equations (20). Equations (21) and (22) constrain the combinations of $\ddot{\mathbf{x}}$, $\dot{\mathbf{x}}$, $\mathbf{x}$, and $\mathbf{f}$ at t and $t + \Delta t$. Equations (23) and (24) constrain the combinations of $\ddot{\mathbf{x}}$, $\dot{\mathbf{x}}$, and $\mathbf{x}$ between t and $t + \Delta t$. When some measured physical quantities are lacking such as $\mathbf{f}$ in the case of experiments, equations (21)–(24) are mandatory. Without equation (25), nonlinear dynamic parameters cannot be estimated.

It was found that α_1 - α_9 are important for successful training. The units of L_2–L_6 and terms in L_1 are different. Therefore, magnitudes of some terms are several digits larger than those of other terms. Optimization algorithms put a priority on larger terms and ignore smaller terms. To prevent this phenomenon, for α_1–α_4, the reciprocals of the maximum measured values of $\ddot{\mathbf{x}}$, $\dot{\mathbf{x}}$, $\mathbf{x}$, and $\mathbf{f}$ are assigned. $\alpha_7 = \alpha_2$ and $\alpha_8 = \alpha_3$ considering the dimensions. The dimension of equation (21) is the same as a force. Assuming height $h_n = 1$, the values are close to a moment. The dimension of equation (22) is the same as an acceleration. The dimension of equation (25) is the same as a force and close to a moment. However, the numerical errors of equations (25) (21) and (22) are large. Therefore, $\alpha_5 = 0.01\alpha_4$, $\alpha_6 = 0.0001\alpha_1$, and $\alpha_6 = 0.01\alpha_4$. These parameters are determined by the trial and error. The same parameters are applicable to other input ground motions and experimental pier cases as explained in Sections 6 and 7. The applicability to other structures is not clear, which is left as future work.

4.3. Optimization. By minimizing the loss function, the parameters of the NN and dynamic model are simultaneously updated. In terms of NN training, an ordinally gradient descent method with momentum was adopted [57, 58]. Early stopping was adopted to shorten the training time. The parameters of NN training are the learning rate lr_1, momentum mt, and the sampling time interval of measurement data t_s. The effects of the three parameters are discussed in Sections 6.3.1 and 6.3.2. $\mathrm{lr}_1 = 0.001$ and mt = 0.9 are adopted as the optimal parameters. t_s determines the number of the datasets $T_m = (\ddot{\mathbf{x}}_\mathbf{m}, \dot{\mathbf{x}}_\mathbf{m}, \mathbf{x}_\mathbf{m}, \mathbf{f}_\mathbf{m})$ at each t. There is a tradeoff. The number should be large enough for successful training. However, small t_s drastically increases computational cost. t_s is determined confirming the convergence of the loss and estimated dynamic parameters. t_s does not depend on the characteristics of the response time histories. This point is also discussed in Section 6.3.1.

In terms of dynamic model optimization, a difficulty exists in the local minima of the target nonlinear inverse problem. It was found that simple gradient descent method is not appropriate. Figure 5 explains the difficulty. Data points in a smaller θ_n range are denser than those in a larger θ_n range. At the early stage of training, dynamic parameters are unstable. $\mathbf{f}_\mathbf{y}$ sometimes goes beyond the maximum moments experienced in the seismic event. Optimization algorithms put a priority on a smaller θ_n range because of the number of the data points. As a result, algorithms try to approximate the whole responses using a linear model with elastic stiffness $\mathbf{k}^\mathbf{1}$ (Figure 5(a)). This local minimum is strong. Figure 5(b) explains a similar situation. When $\mathbf{k}^\mathbf{1} \cong \mathbf{k}^\mathbf{2}$, optimization is stacked and gradually transitions to Figure 5(a).

To prevent these problems, original update rules are applied. This study assumes initial parameters $\mathbf{k}_\mathbf{in}^\mathbf{1}$, $\mathbf{k}_\mathbf{in}^\mathbf{2}$, $\mathbf{f}_\mathbf{yin}$, and $\mathbf{c}_\mathbf{in}$. The optimal parameters $\mathbf{k}_\mathbf{up}^\mathbf{1}$, $\mathbf{k}_\mathbf{up}^\mathbf{2}$, $\mathbf{f}_\mathbf{yup}$, and $\mathbf{c}_\mathbf{up}$ are updated with the learning rate lr_2 comparing L inputting the parameters. The updated algorithm is shown in Figure 6. $\mathrm{lr}_2 = 0.001$ is assumed to obtain 0.1% order parameter estimation accuracy. The three rules are as follows: 1. All parameters should be larger than zero. 2. $\mathbf{f}_\mathbf{yin}$ should be smaller than possible yield moments. It is assumed that a few millimeter displacements cause yielding. 3. $\mathbf{k}_\mathbf{up}^\mathbf{1}$ should be at least twice larger than $\mathbf{k}_\mathbf{up}^\mathbf{2}$. $\mathbf{k}_\mathbf{up}^\mathbf{1}$ is usually one digit larger than $\mathbf{k}_\mathbf{up}^\mathbf{2}$. After updating any parameters K_up in Figure 6, if the three conditions do not hold, the update is cancelled. These three rules do not lose generality.

4.4. Estimating Restoring Moments. The discussions above assume measurement data of restoring moment $\mathbf{f}_\mathbf{m}$. In practice, $\mathbf{f}_\mathbf{m}$ is not available because measuring forces is more difficult than measuring other physical quantities. The

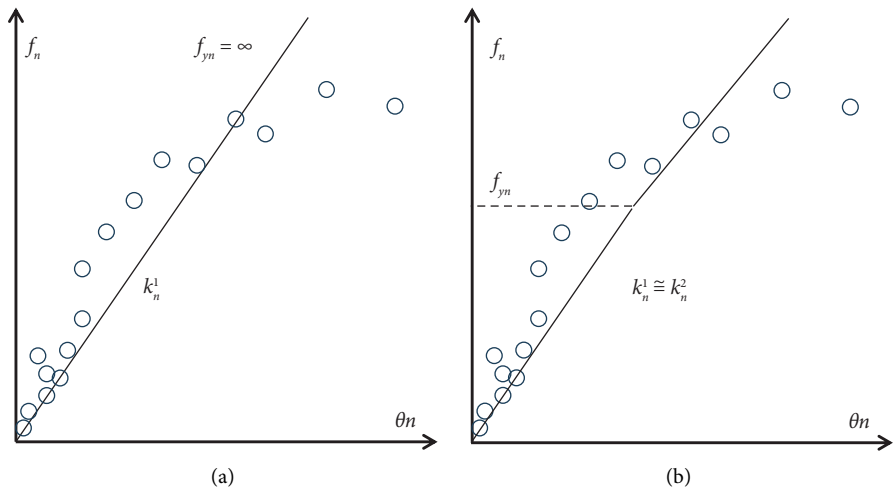

Figure 5: Local minima and plateau of the nonlinear inverse problem. (a) Case of approximating a nonlinear response using a linear model. This case is the strong local minimum. (b) Case of similar elastic and second stiffnesses. This case is a plateau and finally transitions to (a). These cases should be avoided in the optimization process.

$I_{min} \leftarrow$ index (min (L (K_{up}), L ($K_{up} + lr_2K_{in}$), L ($K_{up} - lr_2K_{in}$))

if $I_{min} == 1$

$K_{up} \leftarrow K_{up}$

elseif $I_{min} == 2$

$K_{up} \leftarrow K_{up} + lr_2K_{in}$

elseif $I_{min} == 3$

$K_{up} \leftarrow K_{up} - lr_2K_{in}$

end

Figure 6: Code for updating any dynamic parameter K_{up} using initial K_{in}. The parameters are updated with the learning rate lr_2 comparing loss values L inputting the updated parameters. The update is applied in parallel with the NN parameter updating.

applicability of load cells to high-frequency dynamic responses is not clear [44]. Strains may be converted to forces assuming dynamic properties of materials. However, it was found that without $\mathbf{f_m}$, training tends to be unstable.

To solve the problem, estimated $\widehat{\mathbf{f}}$ is used for dynamic parameter updating. From equation (12), $\widehat{\mathbf{f}}$ is estimated using measured responses with noises $\ddot{\mathbf{x}}_\mathbf{m}$, , $\dot{\mathbf{x}}_\mathbf{m}$:

$$\widehat{\mathbf{f}} = R^{-1}\left(\mathbf{F} - \mathrm{M}\ddot{\mathbf{x}}_\mathbf{m} - \mathrm{C}\dot{\mathbf{x}}_\mathbf{m}\right). \tag{27}$$

From equation (27), $\widehat{\mathbf{f}}$ is a function of C. On the other hand, C is an unknown parameter to be optimized using $\mathbf{f}$. Therefore, this is a mutual optimization process. $\widehat{\mathbf{f}}$ is estimated using C_{up}; C_{up} is updated using $\widehat{\mathbf{f}}$. This process may seem challenging. It is not challenging because equation (27) is the repetition of equation (21). The reason why $\mathbf{f_m}$ is necessary is not clear, possibly because $\mathbf{f_m}$ is fundamental for tuning dynamic parameters.

4.5. Evaluating the Condition of a Pier. In simulations for evaluating the dynamic parameter estimation accuracy of the algorithm, optimized parameters can be compared with ground truth values. For practical application, damage indices are needed to interpret estimation results.

This study proposes two indices: elastic stiffnesses and DFs. The PINN algorithm can output the distributions of elastic stiffnesses and DFs in a pier height direction. Elastic stiffnesses in different cases at the corresponding positions are compared. DF in this study is the ratio between the experienced maximum angle using the reproduced responses and yield angle using the estimated elastic stiffness and yield moment. As a rule of thumb, the previous study indicated that DF < 1.2 is "intact," 1.2 < DF < 1.5 is "suspicious," and 1.5 < DF is "damaged" for the largest Japanese design seismic waves [3, 44, 45]. This study adopts the criteria. The usefulness of damping coefficients for damage assessment is not clear in previous research works [37–39].

5. Simulation Case

5.1. Parameters. This section discusses the characteristic dynamic features of the model shown in Figure 2. Table 1 describes the properties of the simulation model. The model and input ground motion are not the same as the experiments to demonstrate the applicability to other models.

In simulations, the responses of a six-meter pier were obtained with an equal interval $h_n = 1$ m. The pier was divided into six lumped masses concentrated on the measurement positions. A 2 m by 2 m square-section RC pier was assumed. At position $n = 1$, the mass from the foundation to 0.5 m above the measurement position, a 1.5 m height component was considered. At position $n = 2$ to 5, the masses 0.5 m below the position to 0.5 m above the position, 1 m height components were considered. At

Table 1: Dynamic properties of the simulation model.

n	Height h_n (m)	Mass m_n (ton)	Elastic stiffness k_n^1 (N)	Second stiffness k_n^2 (N)	Yield moment f_{yn} (N·m)	Damping coeff. c_n (N/s)
1	1	14.4	$1 \cdot 10^9$	$1 \cdot 10^8$	$5 \cdot 10^6$	$2 \cdot 10^7$
2	1	9.6	$0.9 \cdot 10^9$	$0.9 \cdot 10^8$	$4.5 \cdot 10^6$	$2.2 \cdot 10^7$
3	1	9.6	$1 \cdot 10^9$	$1 \cdot 10^8$	$5 \cdot 10^6$	$2 \cdot 10^7$
4	1	9.6	$1 \cdot 10^9$	$1 \cdot 10^8$	$5 \cdot 10^6$	$2 \cdot 10^7$
5	1	9.6	$1 \cdot 10^9$	$1 \cdot 10^8$	$5 \cdot 10^6$	$2 \cdot 10^7$
6	1	1033.8	$1 \cdot 10^9$	$1 \cdot 10^8$	$5 \cdot 10^6$	$2 \cdot 10^7$

A six-meter height pier with two-meter square sections was divided into six masses. The responses of each mass were obtained. The masses were calculated using the standard RC weight. The dynamic parameters of springs between the masses were assigned referring to the previous research work [39]. The section in a 1-2 m height is damaged; the stiffnesses were smaller by 10%, and the damping coefficient was larger by 10% to test the sensitivity of the algorithm.

position $n = 6$, the masses of the 0.5 m portion of the pier top and decks were considered. The weight of RC about $2.4 \cdot 10^3$ kg/m^3 was assumed. The mass of the deck was ten times larger than that of the pier.

Note that the n-th spring represents an $n-1$ to n m height section of the pier. Referring to previous research [39], elastic stiffness $k_n^1 = 1 \cdot 10^9$ N. Second stiffness $k_n^2 = 1 \cdot 10^8$ N is one-tenth smaller than k_n^1. Yield moment $f_{yn} = 5 \cdot 10^6$ N · m. The yield moments assume that each spring yields with 0.005 rad angle (5 mm displacement). The total elastic displacement at the pier top is 3 cm. This model is softer than a standard RC pier. This is because plastic behaviors do not occur with standard values provided by actual seismic accelerations. The damping coefficient $c_n = 2 \cdot 10^7$ N/s assumes the 10% damping ratio of an equivalent spring-mass-damper model of the pier. To demonstrate the sensitivity of the algorithm, the 1-2 m section of the pier is deteriorated; k_2 is 10% smaller. Some previous research works indicated that damping coefficients of damaged structures increase [38–40]. Therefore, c_2 is 10% larger. The parameters other than h_n and m_n are unknown. The total number of unknown parameters in simulations is 48. The half is the response vectors, and the other half is the dynamic parameters.

Figure 7(a) exhibits the time history of an input seismic acceleration. A JMA Kobe earthquake record was considered [59]. The EW direction was dominant and targeted. The sampling frequency was 100 Hz. All simulated responses were resampled to 100 Hz. This earthquake is near-fault: large intensity up to 800 gal and short duration in 20 s. Small earthquakes may not cause plastic deformations. Figure 7(b) shows the power spectrum of Figure 7(a). Peaks appear from 0.5 to 3 Hz. This study does not depend on modal or frequency analysis. Noises are added to the simulated responses. Referring to the report from a research institute [59], 1 mgal Gaussian noises are added to the accelerations. In adverse conditions, noise levels may increase. The effect of the noises is discussed in Section 6.3.3. Considering the ratios between the maximum acceleration and noise (signal noise ratio, SNR), the same SNR noises were applied to the velocity, displacement, and restoring moment responses.

5.2. Characteristic Features. Figure 8 depicts the time histories of the simulated angles of the springs. The angles of lower springs 1 and 2 of the pier reached the maximum values at the 35 s peaks, while that of upper spring 6 showed many ambiguous peaks. The vibrations gradually attenuate from 50 s. Because of nonlinearity, each response has a residual angle. The residual angle of spring 1 is 0.001 rad, while that of spring 2 is -0.002 rad. The residual angles of the upper springs are almost zero. The residual angles depend on the magnitudes of the angles. However, the relationship is not simple depending on the combination of the dynamic characteristics of the system and input seismic wave. This study avoids this difficulty extracting the mainshock in the 30–50 s time range.

Two features of the link model are discussed here to emphasize the difficulty of the inverse problem. The first feature is that the inclination of the pier is the accumulated angles of the springs from bottom to top. The maximum angle of spring 1 is about 0.028 rad. It corresponds to a 28 mm displacement. On the other hand, the maximum angle of spring 6 is about 0.001 rad, a 1 mm displacement. The angles of lower springs of the pier are the main causes of the displacements of upper masses. Simple estimation of stiffnesses from the displacements of adjacent masses is meaningless.

The second feature is that the elastoplastic behaviors of the springs are varying and discontinuous. Figure 9 shows the hysteretic curves of the springs with an angle on a horizontal axis and a moment on a vertical axis. From Figure 9, springs 1 and 2 show clear nonlinearity. Spring 3 slightly entered a plastic range, which is not clear from the curve. The DF of spring 3 is about 3%. Springs 4–6 were in elastic ranges. The springs gradually entered plastic ranges and increased plastic deformations from bottom to top. In the first peak at 33 s, springs 1 and 2 simultaneously entered the plastic ranges. Spring 1 shows a larger plastic deformation than spring 2. At 36 s after the third peak, spring 3 entered the plastic range. The DFs are varied, and there are time lags of the occurrences of the plastic deformations. This is because after the occurrence of a plastic deformation, a spring absorbs the energy of an input acceleration as much

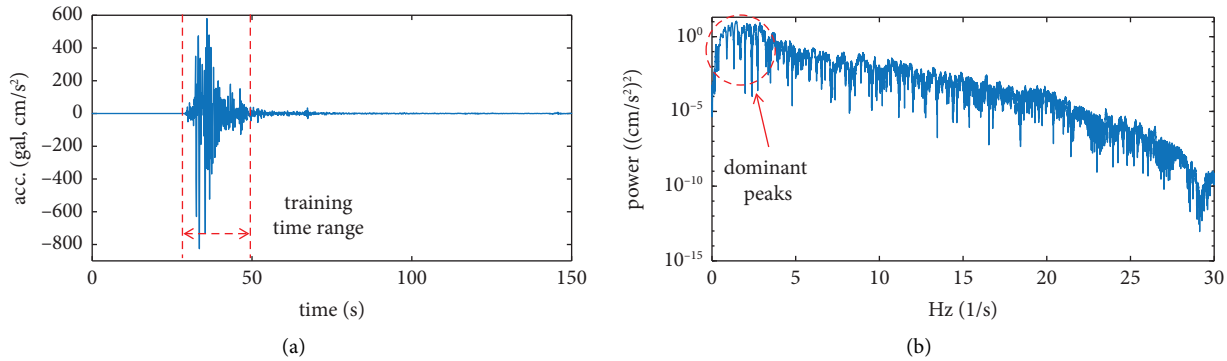

FIGURE 7: Input ground motion for simulations. The JMA Kobe earthquake record in an EW direction was used [58]. The earthquake is a near-fault and short-duration shaking. (a) Time history of the acceleration. 30–50 s is extracted for training. The acceleration is large, reaching about 800 gal. (b) Spectrum of (a). The energy concentrates in 0.5–3 Hz.

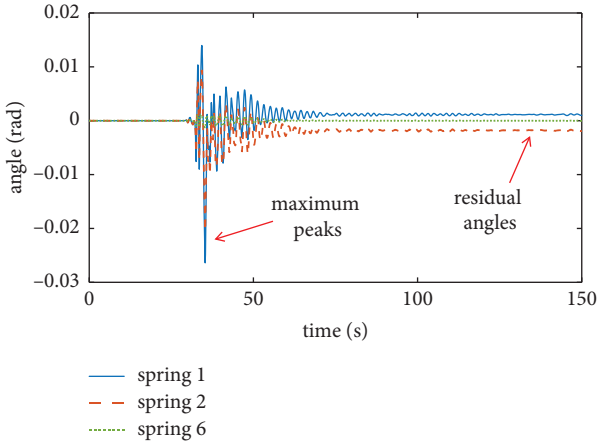

FIGURE 8: Simulated angles of the springs. Springs 1, 2, and 6 are shown as the lower and upper springs of the pier. Maximum peaks of springs 1 and 2 are observed at 35 s, while that of spring 6 is ambiguous. Residual angles occurred because of the nonlinearity of the springs. The residual angles in the lower springs are larger.

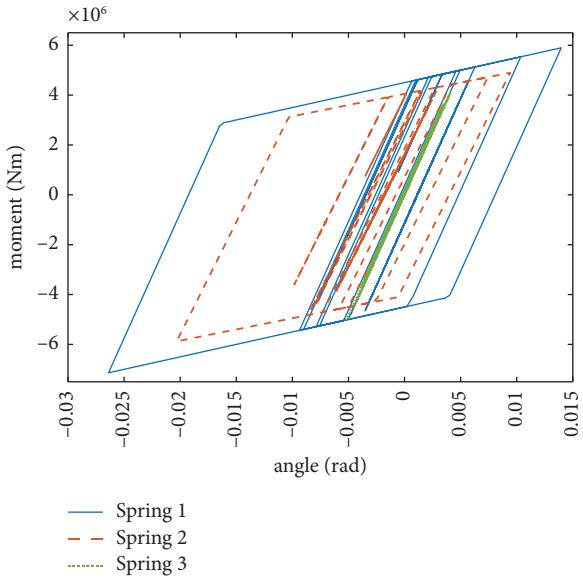

FIGURE 9: Hysteretic curves of the springs. Springs 1, 2, and 3 are shown because springs 4–6 are in elastic ranges. Springs 1 and 2 show large plastic deformations, while that of spring 3 is small. The plastic deformation of spring 1 is larger than that of spring 2.

as possible by widening its hysteretic curve. At a certain deformation, the next spring enters a plastic range. These elastoplastic behaviors correspond to the progresses of local damages in RC bridge piers.

6. Validation by Simulations and Parametric Study

6.1. Computational Environments and Conditions. The proposed algorithm is computationally intensive, which is the largest drawback. In addition to the training technique discussed in Section 6.3.3, GPU parallel computing can be used for facilitating the training process. This study adopts GPU: NVIDIA GeForce GTX 1080 ti and CPU: Intel Core i7-8700K @ 3.7 GHz [12]. This study conducted simulation and training cases in one program for a parametric study. Therefore, all programs were written in MATLAB 2023a [60]. MATLAB is efficient in matrix calculation. However, because of the problem in compatibility between customized functions and the GPU environment, the environment is not fully utilized. It took five to ten hours for one training case. Using the latest GPUs and modified programs, the training time may be twice to one-fifth at the minimum case, which is left as future work [61].

For the initial values of the dynamic parameters, the halves of true elastic stiffnesses $\mathbf{k}^1$, second stiffnesses $\mathbf{k}^2$, and damping coefficients $\mathbf{c}$ are provided to confirm the robustness of the algorithm. Initial yield moments $\mathbf{f}_y$ are the one-tenth of the ground truth values.

6.2. Estimation Results. It was found that all the dynamic parameters of nonlinear springs and dampers are reasonably estimated using simulated responses. This fact demonstrates the power of applying the DL method to the structural identification problem.

Figure 10 and Table 2 summarize the estimation results. Figure 10 shows the curves of the updated dynamic parameters at each epoch. In Figure 10(a), all the dynamic and NN parameters are simultaneously optimized. Figures 10(b)–10(e) are the breakdowns of the curves. There are two types of dynamic parameters: elastic and plastic parameters. Elastic stiffnesses and damping coefficients are the former, and second stiffnesses and yield moments are the latter. From Figures 10(b), 10(c), all the elastic parameters converged. In position $n = 2$, a 10% decrease of first stiffness and a 10% increase of damping coefficients are introduced. From the figures, intact and damaged springs and dampers of the pier are differentiated.

On the other hand, from Figures 10(d), 10(e), plastic parameters show complicated behaviors. From Figure 10(d), the second stiffnesses of lower springs 1–3 of the pier converged, while those of upper springs 4–6 are relatively unstable. This is reasonable because the upper springs are in elastic ranges. Theoretically, the second stiffnesses cannot be estimated. From Figure 10(e), the yield moments converged, and the converged parameters of the springs monotonically decrease. This is because the algorithm outputs the experienced largest moments as the yield moments when the springs are in elastic ranges. Comparing the yield moments is not meaningful; the evaluation of damages using DFs is introduced.

Comparing the curves other than spring 2 in Figure 10, the blue lines of spring 1 converged earlier than springs 4 and 5. Spring 6 is the slowest. This is because the lower springs have larger effects on the responses of the whole system than the upper springs.

Table 2 shows the estimated dynamic parameters. All parameter values at each position, error percentages compared to the ground truth values shown in Table 1, and mean absolute errors (MAEs) of each parameter are listed. The elastic parameters $\mathbf{k^1}$ and $\mathbf{c}$ were accurately estimated with 0.4% and 0.6% errors, respectively. These errors are small considering that the errors of the previous research works are several percent to a few tens percent [20–23]. There is no tendency among the errors.

Plastic parameters $\mathbf{k^2}$ and $\mathbf{f_y}$ DFs of springs 4–6 cannot be evaluated because the springs are in elastic ranges. All the plastic parameters of springs 1 and 2 were accurately estimated within 1% errors, while those of spring 3 are less accurate. This is because the nonlinearity of spring 3 is small, with only a 1.03 DF. MAEs are small. However, interpreting $\mathbf{k^2}$ and $\mathbf{f_y}$ is not straightforward. This study introduced a rule of thumb for DFs. The accuracy of DFs depends on the accuracy of $\mathbf{k^1}$, $\mathbf{f_y}$, and reproduced moment responses. Comparing the estimated DFs, springs 1 and 2 are damaged. The nonlinearity of spring 3 can be ignored. Springs 4–6 show certain DFs. However, the DFs are lower than 1.2 and negligible.

From the results, all the elastic parameters are accurately estimated. The damage conditions related to plasticity and DFs are appropriately evaluated using estimated $\mathbf{k^1}$, $\mathbf{f_y}$, and moment responses.

6.3. Parametric Study. Parametric studies are conducted to demonstrate the robustness and applicability of the algorithm to other measurement and analysis conditions.

6.3.1. Learning Rate and Momentum. To accelerate training, appropriate training parameters are recommended. Figure 11 shows the effects of the learning rate lr and momentum mt on NN training curves. The x axis is an epoch, and the y axis is loss L. In the previous subsection, lr = 0.001 and mt = 0.9 were adopted. The red curve monotonically decreased during the training. L converged at about a 1300 epoch. Pulses in the curves sometimes appear in other DL research works without applying moving average to the curves [57, 58]. In the case of lr = 0.0001 with the same mt, convergence was slow because of smaller lr. Convergence is also slow in the case of lr = 0.01. This is possibly because the NN parameters oscillated around the optimum, which adversely affected the dynamic parameter estimation process. Comparing the with and without-momentum case with the same lr = 0.001, the effect is clear.

In the red curve in Figure 11, there are two changing points at about 100 and 950 epochs. This phenomenon is characteristic in the proposed PINN. These points correspond to the changing points in Figures 10(b), 10(d), 10(e) at the same epochs. The decrease before the 100 epoch is related to the NN parameters because the dynamic parameters were not optimized yet from Figure 10. In some epochs between changing points, the algorithm focuses on the optimization of dynamic parameters; in other epochs, it focuses on NN parameters, or both. The two optimization processes are interdependent. Without regularization factors, training is not balanced and stacked during the update of the parameters.

6.3.2. Numbers of NN Layers and Data Points. Target ranges of the time histories were extracted as explained in Figure 7(a). Following the time interval t_s, samples were evenly extracted from the time histories. Quantities at two times t and $t + \Delta t$ and n positions constitute a data vector $T_m = \{\ddot{\mathbf{x}}_\mathbf{m}(t), \ddot{\mathbf{x}}_\mathbf{m}(t + \Delta t), \dot{\mathbf{x}}_\mathbf{m}(t), \dot{\mathbf{x}}_\mathbf{m}(t + \Delta t), \mathbf{x}_\mathbf{m}(t), \mathbf{x}_\mathbf{m}(t + \Delta t), \mathbf{f}_\mathbf{m}(t), \mathbf{f}_\mathbf{m}(t + \Delta t)\}$. T_m at different times t constitutes a training dataset.

The proposed algorithm has the power of estimating dynamic parameters using small training data points. Figure 12 exhibits the sampled points of the pier top acceleration with time intervals $t_s = 0.5$ s and $t_s = 0.1$ s, respectively. The number of the datasets is 40 in the case of $t_s = 0.5$ s. These t_s were selected confirming the convergence of the estimated dynamic parameters while suppressing the calculation costs. Even though the number of the vectors is 40, considering the numbers of the quantities, positions, and time t and Δt, the number becomes 1,920. From the results, it is implied that 40 points can provide the information of the behaviors of the bilinear springs. Most peaks in the responses are missed with $t_s = 0.5$ s. Nevertheless, the small number of the response samples was enough for accurately estimating the dynamic parameters.

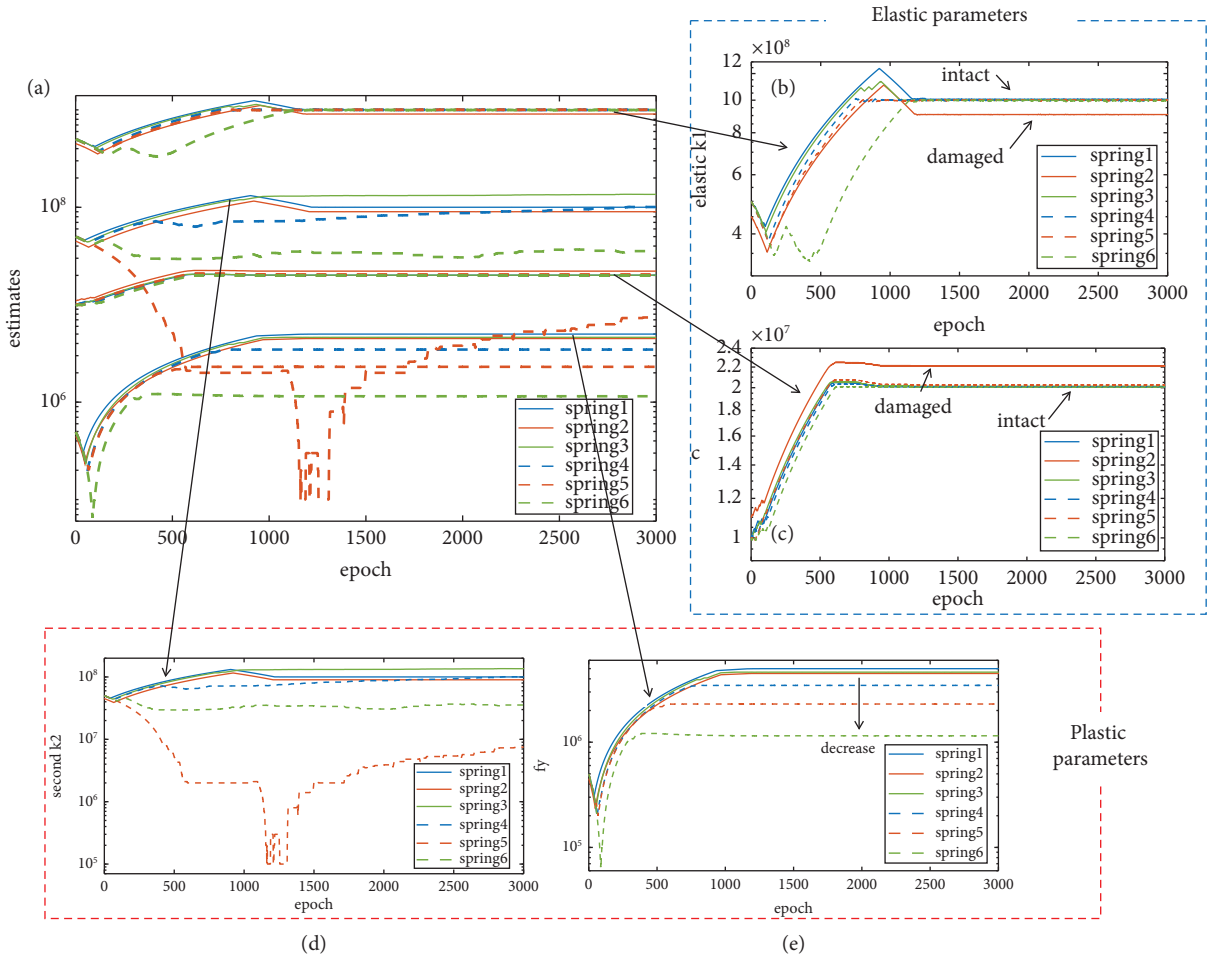

FIGURE 10: Curves of the updated dynamic parameters at each epoch. All the dynamic and NN parameters are simultaneously optimized. (a) All parameter curves of springs 1–6. (b–e) The breakdowns of the curves. (b, c) Elastic and (d, e) plastic parameters. (b) Elastic stiffnesses. (c) Damping coefficients. (d) Second stiffnesses. (e) Yield moments. The elastic parameters accurately converged differentiating the damage conditions. The plastic parameters show complicated behaviors because springs 4–6 are not in plastic ranges. DFs are essential for evaluating the nonlinearity.

TABLE 2: Dynamic parameter estimation results.

n\estimates	$\mathbf{k}^1$ (N, error %)	$\mathbf{k}^2$ (N, error %)	$\mathbf{f}_y$ (N·m, error %)	$\mathbf{c}$ (N/s, error %)	DF (–)
1	$1.007 \cdot 10^9$ (+0.7%)	$1.001 \cdot 10^8$ (+0.1%)	$4.995 \cdot 10^6$ (+0.1%)	$2.008 \cdot 10^7$ (+0.4%)	5.278 (+0.7%)
2	$0.906 \cdot 10^9$ (+0.7%)	$0.901 \cdot 10^8$ (+0.1%)	$4.496 \cdot 10^6$ (-0.1%)	$2.211 \cdot 10^7$ (+0.5%)	4.060 (+0.7%)
3	$1.000 \cdot 10^9$ (+0.0%)	$1.359 \cdot 10^8$ (+35.9%)	$4.650 \cdot 10^6$ (−7.4%)	$2.012 \cdot 10^7$ (+0.6%)	1.119 (+8.0%)
4	$0.998 \cdot 10^9$ (+0.2%)	$1.007 \cdot 10^8$ (–%)	$3.465 \cdot 10^6$ (–%)	$2.010 \cdot 10^7$ (+0.5%)	1.083 (–%)
5	$1.002 \cdot 10^9$ (+0.2%)	$0.075 \cdot 10^8$ (–%)	$2.305 \cdot 10^6$ (–%)	$2.026 \cdot 10^7$ (+1.3%)	1.102 (–%)
6	$0.995 \cdot 10^9$ (+0.5%)	$0.355 \cdot 10^8$ (–%)	$1.150 \cdot 10^6$ (–%)	$2.004 \cdot 10^7$ (+0.2%)	1.046 (–%)
Mean absolute error	0.4%	12.0%	2.5%	0.6%	3.1%

All the dynamic parameters and DFs of the springs are listed with mean absolute errors (MAEs) for each parameter. The plastic parameters and DFs of springs 4–6 cannot be evaluated because the springs were in elastic ranges. All the MAEs of the elastic parameters are small from the results compared to previous research works [20–23]. The DFs were reasonably estimated to judge the conditions of the pier sections.

Appropriate combinations of t_s and the numbers of perceptrons p and NN layers q should be adopted for successful training. Table 3 summarizes loss value L with different t_s, p, and q combinations. Figure 11 suggests that $L = 1 \cdot 10^{-7}$–$1 \cdot 10^{-9}$ is necessary for the successful dynamic parameter estimation. Increasing p, q with fixed t_s, L converged to the minima. To reproduce high-frequency complex responses, p and q should be large enough. The larger the parameters are, the higher the representation ability of the NN is.

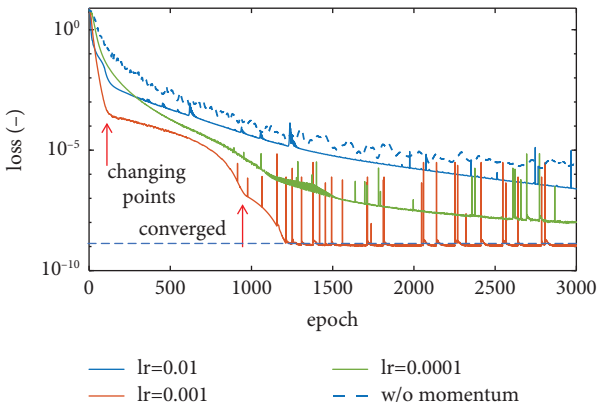

FIGURE 11: Training curves changing training parameters. To facilitate training, the appropriate combination of learning rate and momentum is recommended. Two changing points indicate the inter-dependence of NN and dynamic parameter updating processes.

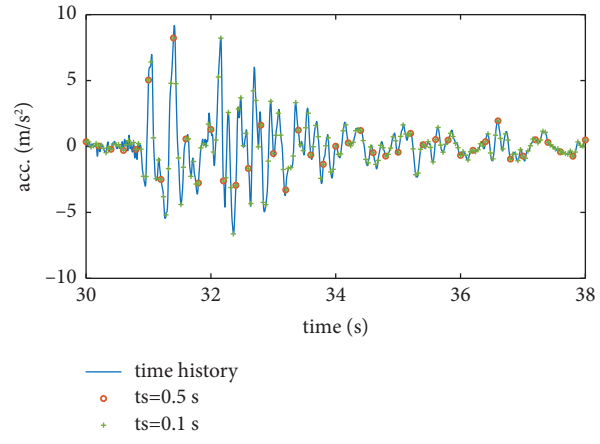

FIGURE 12: Sampled points for training data. Time intervals 0.5 and 0.1 s are compared. Most peaks are lost with the 0.5 s sampling time interval, while they are reproduced with the 0.1 s time interval. However, the dynamic parameter estimation results were the same, indicating that the algorithm can estimate the dynamic parameters with a small number of the points, and the appearances of the reproduced responses are not important.

However, training time is not negligible. With $t_s = 0.5$ s, $p = 500$, and $q = 15$, the training time was around five hours. With $t_s = 0.1$ s, $p = 1000$, and $q = 30$, the training time was about two days. In hazardous situations after earthquakes, quick condition assessment is better. The latest GPUs can halve the training time. This point is left for future work.

6.3.3. Measurement Noises. The algorithm is robust to measurement noises. Table 4 compares the MAEs of the dynamic parameters with different noise levels from 0.1 to 10 mgal. The results in Section 6.2 assume the possible noise level of accelerometers, 1 mgal. From Table 4, the results did not change regardless of the different noise levels. It may seem strange that the error of $\mathbf{k}^2$ is 0.6%, with the 10 mgal noise, while it is 13.1%, with the 0.1 mgal noise. With different simulation conditions, the error of $\mathbf{k}^2$ changed because the estimation was unstable. Therefore, this study focuses on DFs for evaluating nonlinearity.

The algorithm is applicable to a 10 mgal noise. 10 mgal noises are high considering the performances of accelerometers [59]. Referring to the concept of SN ratios, the same algorithm is applicable to one-tenth smaller earthquakes. 50 to 100 gal moderate earthquakes have occurred regularly and are easily measured in seismic-prone countries [1, 2]. With these earthquakes, plastic deformations may not occur. However, small ground motions may be used for shortening training time. Using small ground motions, only elastic parameters are updated. Fixing the elastic parameters, only plastic parameters can be updated. It was observed that this method reduced training time by about 20%. Another usage is that the deterioration of a pier can be tracked using long-term monitoring data though this approach requires monitoring costs and labors.

6.3.4. Input Ground Motions. The algorithm is also robust to various input ground motions. The results shown in Table 2 are using Kobe earthquake. The algorithm is also validated using Tohoku earthquake in 2011, Japan, and El-Centro earthquake in 1940, United States [62, 63]. Kobe and El-Centro earthquakes are near-fault short-duration ground motions, while Tohoku earthquake is an off-shore long-duration ground motion as shown in Figure 13. Kobe and Tohoku earthquakes have two main peaks, while El-Centro earthquake has one main peak at the beginning. Longer earthquakes with more peaks may be favorable for the algorithm. Appropriate time ranges with the same t_s were selected confirming the numbers of the training data points were not smaller than that of Kobe earthquake as shown in Figure 7(a) and Figure 13.

Table 5 compares the MAEs of the dynamic parameters using different earthquakes. The results were similar; no tendency was observed. The results indicated that the algorithm can estimate the parameters regardless of the types of the ground motions.

6.3.5. Measured Physical Quantities. Reducing the number of the required physical quantities of measurement data is important for practical application. The algorithm requires four quantities: acceleration, velocity, displacement, and restoring moment. However, by inputting zeros to regularization factors α_1–α_4 in equation (20), any observations can be ignored in L. This method can reduce the required measurement physical quantities.

Table 6 summarizes the effects of reducing the quantities. Omitting two quantities caused failures in training processes except for case 1 where omitting velocities and displacements did not have any effect on training. Accelerations are integrated to velocities and displacements in equations (23) and (24). Displacements are related to restoring moments via bilinear models in equation (25). Velocities and displacements are intermediate variables. Therefore, these observations are not important when other observations are provided. In case 2 omitting accelerations, parameters finally

Table 3: Effects of the numbers of perceptrons and layers on the loss values with different training data sampling time intervals.

Parameters	$p = 250$, $q = 5$ ($t_s = 0.5$ s)	$p = 500$, $q = 15$ ($t_s = 0.5$ s)	$p = 1000$, $q = 30$ ($t_s = 0.5$ s)	$p = 250$, $q = 5$ ($t_s = 0.1$ s)	$p = 500$, $q = 15$ ($t_s = 0.1$ s)	$p = 1000$, $q = 30$ ($t_s = 0.1$ s)
Loss L	$1.6 \cdot 10^{-3}$	$1.1 \cdot 10^{-9}$	$1.2 \cdot 10^{-9}$	$1.2 \cdot 10^{-3}$	$2.1 \cdot 10^{-6}$	$5.6 \cdot 10^{-8}$

The loss converged increasing the numbers of the perceptrons and layers with fixed intervals; the representation ability of the NN increases. The numbers should be larger enough for given sampling time intervals to reproduce the complexities of the time histories.

Table 4: Effects of the measurement noises on the MAEs of the dynamic parameters.

Noise (mgal, dB)	$\mathbf{k}^1$ (MAE %)	$\mathbf{k}^2$ (MAE %)	$\mathbf{f}_y$ (MAE %)	$\mathbf{c}$ (MAE %)	DF (MAE %)
0.1, −67	0.3	13.1	2.7	0.5	3.1
1, −57	0.4	12.0	2.7	0.6	3.1
10, −47	0.6	0.6	2.7	0.6	2.9

The noises changed from 0.1 to 10 mgal. 1 mgal is the noise of typical accelerometers. 10 mgal is unreasonably high. The algorithm is robust to the different levels of the noises.

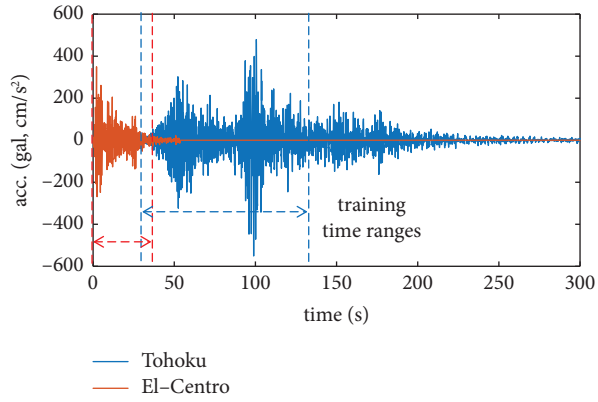

Figure 13: Input ground motions. Tohoku and El-Centro earthquakes are considered as off-shore long-duration and near-fault short-duration waves. Large earthquakes were targeted. Appropriate time ranges and sampling time intervals were selected to process training data.

Table 5: Effect of ground motions on the MAEs.

Ground motion	$\mathbf{k}^1$ (MAE %)	$\mathbf{k}^2$ (MAE %)	$\mathbf{f}_y$ (MAE %)	$\mathbf{c}$ (MAE %)	DF (MAE %)
JMA Kobe	0.4	12.0	2.7	0.6	2.7
Tohoku	0.5	6.7	1.3	0.9	1.3
El-Centro	0.5	12.2	1.1	0.8	1.5

No tendency was observed. The algorithm is robust to the different types of the ground motions.

converged to the ground truth values. However, the training time was about ten times larger than that of the with-acceleration case. Accelerations can be estimated from velocities and displacements though differentiating the quantities may not be easy. In case 3, omitting restoring moments caused a failure in training. However, using estimated restoring moments discussed in Section 4.4 outputted the same results as the with-restoring-moment case. It is inferred that measured restoring moments played a key role in the training and parameter estimation.

For practical application without restoring moments, measuring accelerations, velocities, and displacements is mandatory. Novel measurement technologies for these quantities have been rapidly developed as discussed in Introduction Section. In the future, using strains or other force-related quantities, the combination of accelerations and forces may become a favorable choice.

7. Validation by Experiments

The applicability of the algorithm was demonstrated using the responses of a full-scale RC bridge pier subjected to ground motions via a shaking table. Discussion points here are the applicability of the assumed dynamic model and estimation method to real responses and effect of real measurement conditions. Hysteretic curves of real piers were more complicated than those of the bilinear model as reported in [36, 64]. This simplification may cause a problem.

Table 6: Effects of the combinations of measured physical quantities.

Case	Acceleration	Velocity	Displacement	Restoring moment	Estimation results and remarks
1	✓	×	×	✓	✓ No effect
2	×	✓	✓	✓	✓ Slow convergence
3	✓	✓	✓	×	× Not successful ✓ no effect using estimated restoring moment

The four quantities were considered. Remarks on training time and accuracy of estimation results are listed. The algorithm is amenable to the cases lacking different quantities. The set of the acceleration, velocity, and displacement estimating the restoring moment is feasible in actual measurements.

Ground truth parameters of the damaged piers are not known. Referring to possible stiffnesses as initial values, estimated parameters are related to inspected damage conditions in different cases.

7.1. Measurement Conditions. A 7.5 m height RC bridge pier was considered. The pier has a circular section and rectangular top. The weights of the decks were applied to the top via bearings. Figure 14 depicts the configuration of the measurements. Four accelerometers were placed on the foundation to measure input accelerations. The accelerations and displacements of the NS and EW faces of the pier and corners and sides of the top were measured. Intervals in a height direction were about 2 m. Servo-type accelerometers were attached to the red points in Figure 14. Displacements were measured using wires connected to the frame fixed to the table. Because velocity measurements are not common in practice, only two servo-type velocity meters were attached to the foundation and pier top. All the measured responses were 3D, and the sampling frequencies were 200 Hz. The strains of vertical rebars were also monitored using embedded strain gauges for judging the yielding of the rebars.

Figure 15 compares the measured velocity at the top and average of the integrated accelerations on the top after detrending from 8 s to the last. The peaks and waveforms are reproduced by the integration. Therefore, the integrated accelerations are used for measured velocities. There are gaps around 20 s. This is possibly because of the 3D motions of the pier. There are gaps among the accelerations in different positions on the top. Therefore, all the responses at the same height were averaged to remove the effects of the 3D motions. Damages may be localized in horizontal sections using the differences among the responses.

The pier was subjected to multiple ground shakings. Two cases are compared in this study: after the first and third shakings. The input ground motion was Kobe earthquake, the same earthquake as the simulations. However, a measured station was different (Takatori station). The intensity of the wave was about 20% larger than the simulation wave. In the third shaking, to accelerate the deterioration, the weights of the decks were increased by 20% by putting additional weights.

Figure 16 compares the 0–2 m height conditions of the pier after the two cases. Figure 17 compares the inspection results of cracks and collapses of concrete after the two cases. In case 1, cracks appeared around the circumferences of the pier. Small pieces popped out around the crack. In case 2, cracks were developed in the height direction. The concrete was collapsed. The rebars yielded in the first case, and strains were doubled in the second case. In practice, the pier should be inspected and repaired if necessary in the first case and judged as damaged and replaced in the second case [43].

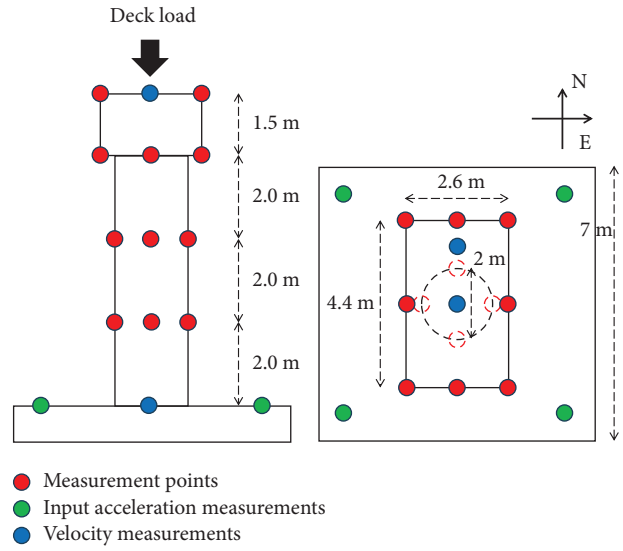

Figure 14: Measurement configuration. A sensor network was introduced to monitor 3D motions of the pier. Accelerations and displacements were measured at the red points using servo-type accelerometers and wires fixed to a surrounding frame. Input accelerations were measured at the green points on the foundation. Velocity meters were installed on the two blue points.

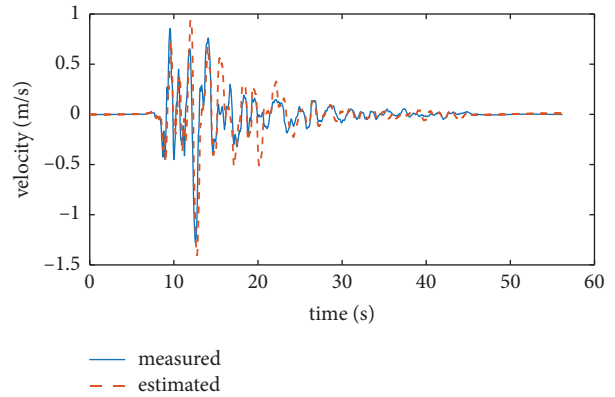

Figure 15: Comparison of the measured velocity at the pier top and estimated velocity using the averaged accelerations on the top. The estimated one matches the measured one at around the 10 s main peaks, which shows the validity of the velocity estimation.

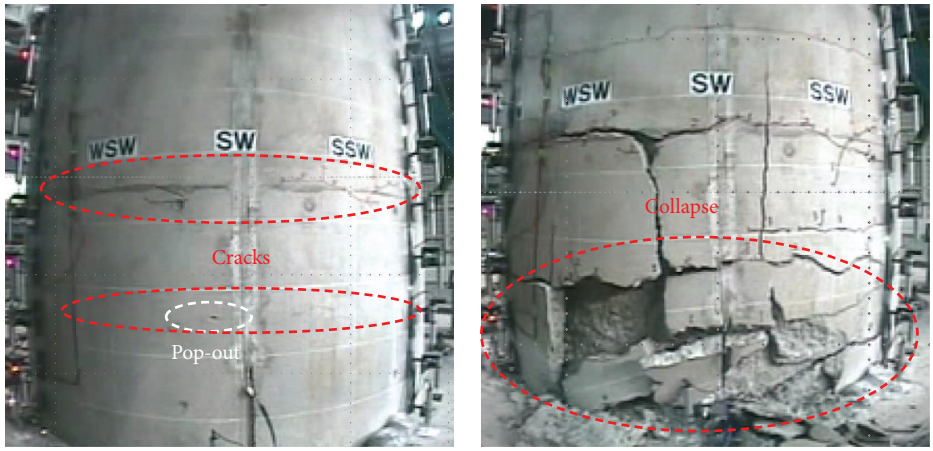

(a) (b)

FIGURE 16: Photos of 0–2 m height conditions of the pier after the first and third shakings. Multiple ground shakings were applied to the pier via a shaking table to accelerate the deterioration. (a) After the first shaking (case 1). Horizontal cracks around the circumferences and a pop-out on the crack were observed. (b) After the third shaking (case 2). The concrete was collapsed, causing a dangerous situation.

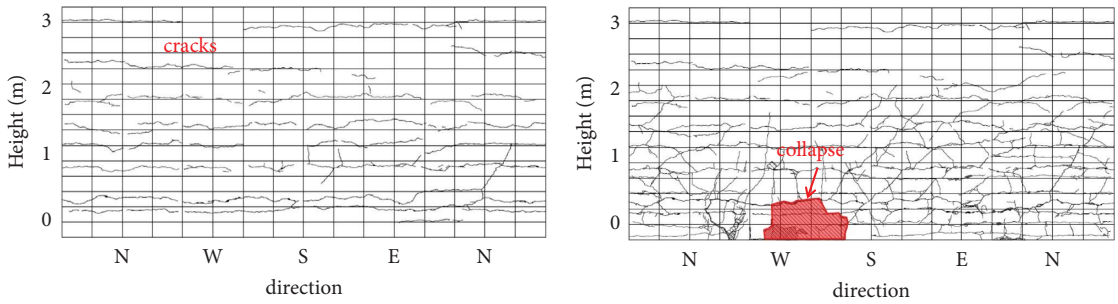

(a) (b)

FIGURE 17: Inspection results of the pier surfaces after the two cases. (a) Case 1. (b) Case 2. Vertical cracks were developed in case 2, and the collapse of concrete occurred in the bottom of the pier.

7.2. Analysis Conditions. Four sections 0–2 m, 2–4 m, 4–6 m, and 6–7.5 m in the height direction between the measurement points were evaluated. Referring to the design drawings, masses were assigned to the boundaries of the sections. The number of unknown parameters is 32. The half is responses. The other half is dynamic parameters.

All the responses were resampled to 100 Hz. Following the reference, the responses in horizontal directions were extracted and converted to responses in a principal direction [44]. Principal direction $\theta_p = 196^\circ$ in case 1 and $\theta_p = 196^\circ$ in case 2, almost directing west. Note that depending on the arrangements of sensors and wire directions, the signs of the data may change. Relative accelerations and velocities were estimated by subtracting the accelerations and velocities of the foundation.

Initial dynamic parameters were the same as the ground truths in the simulations. Restoring moments were estimated as explained in Section 4.4. The same training parameters were adopted. Without early stopping, the parameters became unstable. Some parameters converged to ten times larger values, and other parameters converged to almost zeros. This phenomenon may be overfitting. The reason may be the gap between the assumed and actual hysteretic curves. The numbers of the perceptrons, layers, and sampling time interval were optimized confirming the convergence of the estimation results: $p = 1000$, $q = 30$, and $t_s = 0.005$ s. The number of the data points was larger than that of the simulation cases possibly because of the gap in the hysteresis curves. To increase the number of the data points, p and q should be increased. Training time was about ten hours for the adopted architecture, number of data points, and unknown parameters.

7.3. Results. Figure 18 summarizes the dynamic parameter estimation results. The distributions of elastic stiffnesses $\mathbf{k}^1$ and ductility factors DFs along the pier height are compared between the two cases. These distributions are unique in this study.

The parameters show clear tendencies corresponding to the damage conditions of the pier. Figure 18(a) compares $\mathbf{k}^1$ along the pier height. In the two cases, $\mathbf{k}^1$ varies in the height direction. Small k_4^1 at the top may be because of the bearings and decks. The structural property is different. $\mathbf{k}^1$ at 2–6 m is 20% to 30% smaller than k_1^1

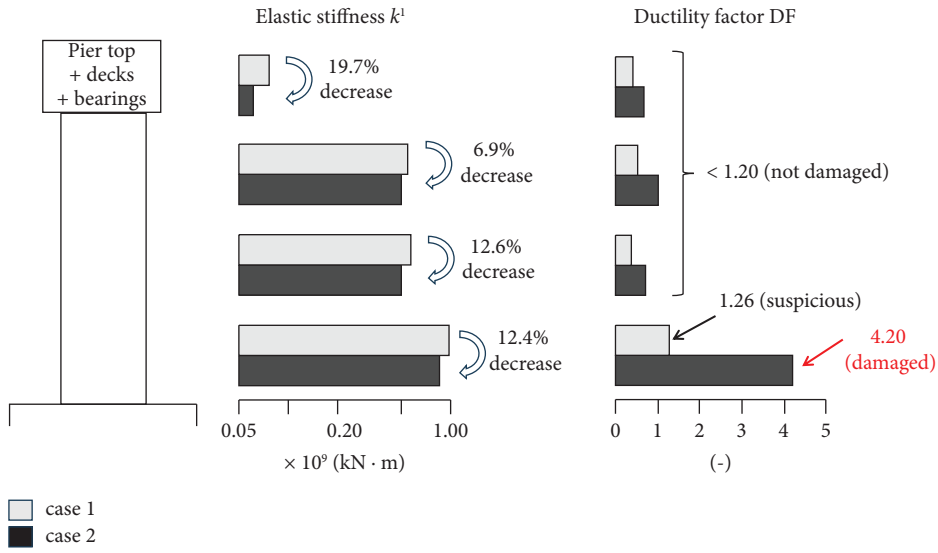

FIGURE 18: Dynamic parameter estimation results of a full-scale RC bridge pier. Case 1 after the first shaking and case 2 after the third shaking in Figures 16 and 17 are compared. The distributions of the elastic stiffnesses and DFs along the pier height are shown. The elastic stiffnesses of all the sections decreased by 12–20%. On the other hand, the DF significantly increased from 1.3 to 4.2 only at the bottom of the pier, while other DFs were lower than 1.2. The overall decrease of the elastic stiffnesses is inferred to be the effect of the cracks of the concrete and yielding of the rebars. The local increase of the DF is the effect of the collapse of the concrete. The damages are localized and quantitatively evaluated as shown in the distributions.

at 0–2 m. There are two possible reasons: the first reason is related to the rebar arrangements. The rebars in the bottom of the pier were L-shaped to prevent the pullout of the rebars. The second reason is related to stress conditions. Because the stress in the bottom of the pier is larger than that of the top, the stress conditions in the horizontal sections may be different, which may change the equivalent stiffnesses. This study did not conduct detailed structural analysis. The validation of the analysis is not easy either. In practice, the shapes of sections may change in a height direction. Therefore, the comparison of $\mathbf{k}^1$ in the height direction is not meaningful.

Comparing $\mathbf{k}^1$ between the two cases, the effects of the damages are clear. $\mathbf{k}^1$ at 0–4 m decreased by 12-13%. The collapse of the concrete is localized at the 0–2 m height. Therefore, these decreases are inferred to be the effects of the developed cracks and yielded rebars. $\mathbf{k}^1$ at 4–6 m decreased by 7%. This result suggests that the two types of the damages are more severe in the lower part of the pier. The decrease at the top is about 20%. The fixed conditions of the bearings may change because of the excessive external forces.

Comparing the DFs, the effect of the collapse of the concrete is revealed. The DFs at 2–7.5 m is lower than 1.2 in both cases. These DFs indicate that the pier did not cause plastic deformations. The DF in case 1 at 0–2 m is about 1.3. Referring to the rule of thumb, this DF suggests that the section may be deteriorated. The DF in case 2 is about 4.2. This DF corresponds to a large plastic deformation and severe damage condition. This significant DF increase is owing to the collapse of the concrete.

The advantages of this study exist in the localization and quantification of nonlinear damages. The DF reported in the previous study was about 5.6 based on the displacement of the pier top [44]. That DF was global. This study estimated the local DFs. The angles were accumulated to constitute the displacement at the top. Therefore, local DFs are usually smaller than a global DF. The pier at 2–7.5 m did not observe a plastic deformation. However, these linear displacements were included in the global DF. Furthermore, the timings of the largest deformations at the springs were not the same. Therefore, this study claims that the local DFs are more precise than the global DF.

Estimated dynamic parameters other than shown in Figure 18 are second stiffnesses and damping coefficients. The second stiffnesses were one-tenth smaller than the elastic stiffnesses. The damping coefficients of case 2 were one-tenth smaller than those of case 1 and the simulations. This is possibly because the concrete was collapsed and peeled off from the structure in case 2, while the cracks in the concrete absorbed the energy in case 1. Previous discussions may not be enough to use these parameters as damage indices.

8. Discussions

This study addressed nonlinear MDOF dynamic system identification based on the PINN and RC bridge pier model assuming bilinear rotational springs and dampers. After the derivation of the PINN optimization algorithm, the effects of the NN architectures, training parameters, t_s, noises, ground motions, and measured physical quantities were analyzed. The algorithm is robust to the effects of the noises and ground motions with the appropriate NN parameters and quantities. The errors of the estimated $\mathbf{k}^1$, $\mathbf{c}$, and DFs in the simulations were 0.4%, 0.6%, and 3.1%, respectively. Utilizing full-scale RC bridge pier shaking table experiments,

the algorithm revealed the distributions of $\mathbf{k}^1$ and DFs along the pier height in the different cases, representing the conditions of the pier. It is inferred that $\mathbf{k}^1$ is related to cracks in concrete and yielding in rebars, and DF is related to the collapse of the concrete. The algorithm localized and quantitatively evaluated the different damage types.

Required training time and measurement data are the bottlenecks. Training time can be reduced using high-end GPUs. Latest NN architectures such as deep residual convolutional neural networks (CNNs) and attention mechanisms may facilitate the training process and increase prediction accuracy [65–67]. To omit restoring moments, accelerations, velocities, and displacements are needed. Dense displacement measurement may be possible using cameras and laser technologies. Strains are easy to be measured though appropriate material properties are needed to convert them to forces.

Now that local damages are estimated, appropriate indices for evaluating pier conditions should be discussed. The $\mathbf{k}^1$ decrease compared to an initial condition and DF per meter in a height direction are the possible indices. For future work, crack and spalling detection using images by DL can be used to increase accuracy.

The validity of the estimated stiffnesses, yield moments, damping coefficients, and ductility factors should be validated by detailed structural analysis such as FEM and analytical RC column models.

The bilinear hysteretic model may be advanced to improve the accuracy of the parameter estimation. The stability of training was sensitive to the number of unknown hysteretic parameters. However, actual curves showed complicated fluctuating trajectories. Additional constraints may be needed to apply other hysteresis models.

The algorithm can be applied to 3D problems using 3D observations and governing equations. The differences of the responses at the same height suggest that the damages can be localized in horizontal sections. By Bayes' theorem, the algorithm can consider the uncertainty of estimated dynamic parameters. To increase the number of nonlinear springs, measurement points should be added. Without the observations, the problem becomes ill-posed. Focusing on linear problems, the number of springs may be increased. Shear deformations and foundation pile motions can be considered though it will increase the number of unknown parameters.

The PINN has a potential to be applied to other structural problems [68]. The applicability of regularization factors should be confirmed for other problems. Parameter updating rules may also be customized.

9. Conclusions

In this study, a damage identification algorithm for RC bridge piers was proposed based on PINN using seismic responses. The target of this study is all nonlinear MDOF dynamic system identification. A bilinear-rotational-spring-and-damper model for an RC bridge pier was assumed. PINN equations were derived. The estimation scheme for a large number of dynamic parameters up to about 50 was developed. The algorithm was validated using simulations, showing that the errors of estimated elastic stiffnesses, damping coefficients, and DFs are 0.4%, 0.6%, and 3.1%, respectively. The results using full-scale shaking table experiments demonstrated that the distributions of elastic stiffnesses and DFs along the pier height not only indicate the locations and extents of damages but also imply damage types such as cracks and yielding of rebars and collapses of concrete.

This study presented the potential of the PINN to structural identification problems. Training time reduction and measurement techniques are important directions for future work. Parallel computing environments should be advanced for shortening training time. The quantum neural network utilizes quantum theory to efficiently learn features and reduce training time compared to NNs [69, 70]. The network may be useful for our problem. Acceleration, velocity, and displacement data are needed. Latest camera, laser, and strain measurement technologies may alleviate the labors of collecting the measurement data. The estimated dynamic parameters may be validated using detailed FEM and analytical RC column models. The architecture of the NN may be improved. The number of DOF, dimension of the dynamic model, and complexity of the hysteretic model may be increased with additional constraints for advanced condition assessment [71].

Data Availability

The authors do not have permission to share the measurement data provided in this article.

Conflicts of Interest

The authors declare that there are no conflicts of interest regarding the publication of this article.

Acknowledgments

This research was financially supported by the Japan Science and Technology Agency, Japan (grant number: 23K19133).

References

[1] The World Bank, "Syria earthquake 2023: rapid damage and needs assessment (RDNA)," 2023, https://documents1.worldbank.org/curated/en/099093003162314369/pdf/P17217110e2b4a60b40a5940f0793f8a0d24.pdf.

[2] Ministry of Land, Infrastructure, and Transport and Tourism, "Great East Japan earthquake," 2023, https://www.mlit.go.jp/page/kanbo01_hy_001411.html.

[3] Ministry of Land, Infrastructure, and Transport and Tourism, "Road bridge design standard (in Japanese)," 2023, https://www.mlit.go.jp/road/sign/kijyun/pdf/2017.0721hashikouka.pdf.

[4] Elsevier, *Topics: Multihop Wireless Network*, Elsevier, Netherlands, 2023.

[5] X. Pan, T. Y. Yang, Y. Xiao, H. Yao, and H. Adeli, "Vision-based real-time structural vibration measurement through deep-learning-based detection and tracking methods," *Engineering Structures*, vol. 281, Article ID 115676, 2023.

[6] S. Ri, M. Fujigaki, and Y. Morimoto, "Sampling moiré method for accurate small deformation distribution measurement," *Experimental Mechanics*, vol. 50, no. 4, pp. 501–508, 2010.

[7] T. Yamashita and K. Mitani, "8K extremely-high-resolution camera systems," *Proceedings of the IEEE*, vol. 101, no. 1, pp. 74–88, 2013.

[8] H. S. Park, H. M. Lee, H. Adeli, and I. Lee, "A new approach for health monitoring of structures: terrestrial laser scanning," *Computer-Aided Civil and Infrastructure Engineering*, vol. 22, no. 1, pp. 19–30, 2007.

[9] R. Nasimi and F. Moreu, "A methodology for measuring the total displacements of structures using a laser–camera system," *Computer-Aided Civil and Infrastructure Engineering*, vol. 36, no. 4, pp. 421–437, 2021.

[10] B. K. Oh, K. J. Kim, Y. Kim, H. S. Park, and H. Adeli, "Evolutionary learning based sustainable strain sensing model for structural health monitoring of high-rise buildings," *Applied Soft Computing*, vol. 58, pp. 576–585, 2017.

[11] TensorFlow, "TensorFlow," 2023, https://www.tensorflow.org.

[12] Nvidia, "Geforce gtx 1080 ti," 2023, https://www.nvidia.com/en-gb/geforce/products/10series/geforce-gtx-1080-ti/.

[13] J. M. Caicedo, S. J. Dyke, and E. A. Johnson, "Natural excitation technique and eigensystem RealizationAlgorithm for phase I of the IASC-ASCE benchmark problem: simulated data," *Journal of Engineering Mechanics*, vol. 130, no. 1, pp. 49–60, 2004.

[14] M. Chang and S. N. Pakzad, "Modified natural excitation technique for stochastic modal identification," *Journal of Structural Engineering*, vol. 139, no. 10, pp. 1753–1762, 2013.

[15] D. M. Siringoringo and Y. Fujino, "System identification applied to long-span cable-supported bridges using seismic records," *Earthquake Engineering and Structural Dynamics*, vol. 37, no. 3, pp. 361–386, 2008.

[16] C. H. Loh and Z. K. Lee, "Seismic monitoring of a bridge: assessing dynamic characteristics from both weak and strong ground excitations," *Earthquake Engineering and Structural Dynamics*, vol. 26, no. 2, pp. 269–288, 1997.

[17] M. T. A. Chaudhary, M. Abe, Y. Fujino, and J. Yoshida, "System identification of two base-isolated bridges using seismic records," *Journal of Structural Engineering*, vol. 126, no. 10, pp. 1187–1195, 2000.

[18] M. T. A. Chaudhary, M. Abe, and Y. Fujino, "Identification of soil-structure interaction effect in base-isolated bridges from earthquake records," *Soil Dynamics and Earthquake Engineering*, vol. 21, no. 8, pp. 713–725, 2001.

[19] J. Yoshida, M. Abe, and Y. Fujino, "Performance of base-isolated bridge during 1995 Kobe earthquake based on observed records," *Doboku Gakkai Ronbunshu*, vol. 1999, no. 626, pp. 37–50, 1999.

[20] M. C. Huang, Y. P. Wang, J. R. Chang, and C. S. Chang Chien, "Physical system identification of an isolated bridge using seismic response data," *Structural Control and Health Monitoring*, vol. 16, no. 2, pp. 241–265, 2009.

[21] H. Ebrahimian, R. Astroza, J. P. Conte, and R. A. de Callafon, "Nonlinear finite element model updating for damage identification of civil structures using batch Bayesian estimation," *Mechanical Systems and Signal Processing*, vol. 84, no. B, pp. 194–222, 2017.

[22] M. N. Chatzis, E. N. Chatzi, and A. W. Smyth, "An experimental validation of time domain system identification methods with fusion of heterogeneous data," *Earthquake Engineering and Structural Dynamics*, vol. 44, no. 4, pp. 523–547, 2015.

[23] Y. Yang, T. Nagayama, and K. Xue, "Structure system estimation under seismic excitation with an adaptive extended kalman filter," *Journal of Sound and Vibration*, vol. 489, Article ID 115690, 2020.

[24] M. Raissi, P. Perdikaris, and G. E. Karniadakis, "Physics-informed neural networks: a deep learning framework for solving forward and inverse problems involving nonlinear partial differential equations," *Journal of Computational Physics*, vol. 378, pp. 686–707, 2019.

[25] M. Raissi, A. Yazdani, and G. E. Karniadakis, "Hidden fluid mechanics: learning velocity and pressure fields from flow visualizations," *Science*, vol. 367, no. 6481, pp. 1026–1030, 2020.

[26] A. D. Jagtap, Z. Mao, N. Adams, and G. E. Karniadakis, "Physics-informed neural networks for inverse problems in supersonic flows," *Journal of Computational Physics*, vol. 466, Article ID 111402, 2022.

[27] E. Haghighat, M. Raissi, A. Moure, H. Gomez, and R. Juanes, "A physics-informed deep learning framework for inversion and surrogate modeling in solid mechanics," *Computer Methods in Applied Mechanics and Engineering*, vol. 379, Article ID 113741, 2021.

[28] Y. Li, P. Ni, L. Sun, and Y. Xia, "Finite element model-informed deep learning for equivalent force estimation and full-field response calculation," *Mechanical Systems and Signal Processing*, vol. 206, Article ID 110892, 2024.

[29] R. Zhang, Y. Liu, and H. Sun, "Physics-guided convolutional neural network (PhyCNN) for data-driven seismic response modeling," *Engineering Structures*, vol. 215, Article ID 110704, 2020.

[30] B. Todorov and A. Muntasir Billah, "Post-earthquake seismic capacity estimation of reinforced concrete bridge piers using Machine learning techniques," *Structures*, vol. 41, pp. 1190–1206, 2022.

[31] A. Fernandez-Navamuel, D. Zamora-Sánchez, A. J. Omella, D. Pardo, D. Garcia-Sanchez, and F. Magalhães, "Supervised deep learning with finite element simulations for damage identification in bridges," *Engineering Structures*, vol. 257, Article ID 114016, 2022.

[32] I. Anastasopoulos, P. C. Anastasopoulos, A. Agalianos, and L. Sakellariadis, "Simple method for real-time seismic damage assessment of bridges," *Soil Dynamics and Earthquake Engineering*, vol. 78, pp. 201–212, 2015.

[33] H. R. Ahmadi, N. Mahdavi, and M. Bayat, "A novel damage identification method based on short time Fourier transform and a new efficient index," *Structures*, vol. 33, pp. 3605–3614, 2021.

[34] R. W. Clough and J. Penzien, *Dynamics of Structures*, McGraw-Hill, Inc, New york, NY, USA, 2nd edition, 1993.

[35] A. K. Chopra, *Dynamics of Structures: Theory and Applications to Earthquake Engineering*, Pearson Prentice Hall, London, UK, 4th edition, 2014.

[36] T. H. Kim, K. M. Lee, Y. S. Chung, and H. M. Shin, "Seismic damage assessment of reinforced concrete bridge columns," *Engineering Structures*, vol. 27, no. 4, pp. 576–592, 2005.

[37] S. Oller and A. H. Barbat, "Moment-curvature damage model for bridges subjected to seismic loads," *Computer Methods in Applied Mechanics and Engineering*, vol. 195, no. 33-36, pp. 4490–4511, 2006.

[38] K. Oide, A. Nakajima, and I. Saiki, "Three dimensional dynamic response analysis of bridge piers by rigid-body-spring model," *Doboku Gakkai Ronbunshu*, vol. 2000, no. 654, pp. 259–270, 2000.

[39] T. Tojo and S. Nakai, "Identification of sway rocking springs and pile damage detection using subspace method," *Journal of Structural and Construction Engineering (transactions of AIJ)*, vol. 87, no. 791, pp. 60–71, 2022.

[40] Y. Okada, Y. Ogawa, M. Hiroshima, and T. Iwatate, "Application of simplified dynamic response analysis and examinations of interection spring and damping factor of existing bridges," *Doboku Gakkai Ronbunshu A*, vol. 65, no. 4, pp. 879–897, 2009.

[41] P. Sideris, A. J. Aref, and A. Filiatrault, "Experimental seismic performance of a hybrid sliding-rocking bridge for various specimen configurations and seismic loading conditions," *Journal of Bridge Engineering*, vol. 20, no. 11, 2015.

[42] X. Chen, Z. Guan, J. Li, and B. F. Spencer, "Shake table tests of tall-pier bridges to evaluate seismic performance," *Journal of Bridge Engineering*, vol. 23, no. 9, 2018.

[43] X. Kang, L. Jiang, Y. Bai, and C. C. Caprani, "Seismic damage evaluation of high-speed railway bridge components under different intensities of earthquake excitations," *Engineering Structures*, vol. 152, pp. 116–128, 2017.

[44] K. Kawashima, T. Sasaki, H. Ukon et al., "Evaluation of seismic performance of a circular reinforced concrete bridge column designed in accordance with the current design code based on E-defense excitation," *Doboku Gakkai Ronbunshu A*, vol. 66, no. 2, pp. 324–343, 2010.

[45] Y. Takahashi and N. Kobayashi, "Quantitative evaluation of seismic response based on simultaneous excitation of 16 RC columns," *Journal of Japan Society of Civil Engineers, Ser A1 (Structural Engineering and Earthquake Engineering (SE/EE))*, vol. 72, no. 1, pp. 176–191, 2016.

[46] K. R. Karim and F. Yamazaki, "Effect of earthquake ground motions on fragility curves of highway bridge piers based on numerical simulation," *Earthquake Engineering and Structural Dynamics*, vol. 30, no. 12, pp. 1839–1856, 2001.

[47] R. P. Dhakal, J. B. Mander, and N. Mashiko, "Identification of critical ground motions for seismic performance assessment of structures," *Earthquake Engineering and Structural Dynamics*, vol. 35, no. 8, pp. 989–1008, 2006.

[48] H. Ebrahimian, R. Astroza, J. P. Conte, and C. Papadimitriou, "Bayesian optimal estimation for output-only nonlinear system and damage identification of civil structures," *Structural Control and Health Monitoring*, vol. 25, no. 4, Article ID e2128, 2018.

[49] A. Roy, A. Santra, and R. Roy, "Estimating seismic response under bi-directional shaking per uni-directional analysis: identification of preferred angle of incidence," *Soil Dynamics and Earthquake Engineering*, vol. 106, pp. 163–181, 2018.

[50] C. C. Spyrakos, "Seismic behavior of bridge piers including soil-structure interaction," *Computers and Structures*, vol. 43, no. 2, pp. 373–384, 1992.

[51] M. Ciampoli and P. E. Pinto, "Effects of soil-structure interaction on inelastic seismic response of bridge piers," *Journal of Structural Engineering*, vol. 121, no. 5, pp. 806–814, 1995.

[52] L. D. Landau and E. M. Lifshitz, *Mechanics*, Butterworth Heinemann, Oxford, UK, 3rd edition, 1976.

[53] R. Feynman, R. Leighton, and M. Sands, *The Feynman Lectures on Physics Volume-: Mainly Mechanics, Radiation, and Heat*, Basic Books Hachette Book Group, New York, NY, USA, 2010.

[54] W. H. Press, S. A. Teukolsky, W. T. Vetterling, and B. P. Flannery, *Numerical Recipes in C the Art of Scientific Computing*, Cambridge University Press, Cambridge, UK, 2nd edition, 1992.

[55] A. Kharab and R. B. Guenther, *An Introduction to Numerical Methods A MATLAB Approach*, Taylor & Francis, Florida, FL, USA, 3rd edition, 2012.

[56] S. Haykin, *Kalman Filtering and Neural Networks*, John Wiley & Sons, Inc, New York, NY, USA, 2001.

[57] C. M. Bishop, *Pattern Recognition and Machine Learning*, Springer Science+Business Media, LLC, New York, NY, USA, 2006.

[58] I. Goodfellow, Y. Bengio, and A. Courville, *Deep Learning*, The MIT Press, Masachesetts, MA, USA, 2016.

[59] Japan Meteorological Agency, "Strong seismic records, Kobe earthquake (Japanese)," 2023, https://www.data.jma.go.jp/eqev/data/kyoshin/jishin/hyogo_nanbu/index.html.

[60] MathWorks, "Matlab," 2023, https://jp.math.works.com/.

[61] PassMark Software, "High end video cart chart," 2023, https://www.videocardbenchmark.net/high_end_gpus.html.

[62] Japan Meteorological Agency, "Strong seismic records, Tohoku earthquake (Japanese)," 2023, https://www.data.jma.go.jp/eqev/data/kyoshin/jishin/110311_tohokuchihotaiheiyouoki/index.html.

[63] Building Performance Standardization Association, "Representative seismic wave records (Japanese)," 2023, https://www.seinokyo.jp/jsh/top/.

[64] J. Su, J. Wang, Z. Li, and X. Liang, "Effect of reinforcement grade and concrete strength on seismic performance of reinforced concrete bridge piers," *Engineering Structures*, vol. 198, Article ID 109512, 2019.

[65] K. He, X. Zhang, S. Ren, and J. Sun, *Deep Residual Learning for Image Recognition*, Computer Vision and Pattern Recognition, Boston, MA, USA, 2015.

[66] H. Chu, W. Wang, and L. Deng, "Tiny-Crack-Net: a multiscale feature fusion network with attention mechanisms for segmentation of tiny cracks," *Computer-Aided Civil and Infrastructure Engineering*, vol. 37, no. 14, pp. 1914–1931, 2022.

[67] J. Chen and Y. He, "A novel U-shaped encoder–decoder network with attention mechanism for detection and evaluation of road cracks at pixel level," *Computer-Aided Civil and Infrastructure Engineering*, vol. 37, no. 13, pp. 1721–1736, 2022.

[68] Y. An, E. Chatzi, S. H. Sim, S. Laflamme, B. Blachowski, and J. Ou, "Recent progress and future trends on damage identification methods for bridge structures," *Structural Control and Health Monitoring*, vol. 26, no. 10, Article ID e2416, 2019.

[69] M. S. I. Sinayskiy and F. Petruccione, "The quest for a quantum neural network," *Quantum Information Processing*, vol. 13, pp. 2567–2586, 2014.

[70] S. Bhatta and J. Dang, "Multiclass seismic damage detection of buildings using quantum convolutional neural network," *Computer-aided Civil and Infrastructure Engineering*, Early view, Longview, TX, USApp. 1–18, 2023.

[71] M. Takahashi and M. Sakaue, "Evaluation of noises for force-balance accelerometers," Technical Rescarch Report, pp. 96–100, Earthquake Research Institute, the University of Tokyo, Tokyo, Japan, 1996.